International Journal of Greenhouse Gas Control 54 (2016) 70–83

Contents lists available at ScienceDirect

International Journal of Greenhouse Gas Control

journal homepage: www.elsevier.com/locate/ijggc

Frictional behaviour and transport properties of simulated fault gouges derived from a natural CO_2 reservoir

Elisenda Bakker[a,*], Suzanne J.T. Hangx[b,1], André R. Niemeijer[a], Christopher J. Spiers[a]

[a] High Pressure and Temperature Laboratory, Department of Earth Sciences, Faculty of Geosciences, Utrecht University, P.O. Box 80.021, 3508 TA Utrecht, The Netherlands
[b] Shell Global Solutions, Kesslerpark 1, 2288 GS Rijswijk, The Netherlands

ARTICLE INFO

Article history:
Received 29 April 2016
Received in revised form 5 August 2016
Accepted 30 August 2016

Keywords:
CCS
Entrada sandstone
Carbonate precipitation
CO_2 leakage

ABSTRACT

We investigated the effects of long-term CO_2-brine-rock interactions on the frictional and transport properties of reservoir-derived fault gouges, prepared from both unexposed and CO_2-exposed sandstone, and from aragonite-cemented fault rock of an active CO_2-leaking conduit, obtained from a natural CO_2 field (Green River, Utah). Direct shear experiments (5–90 MPa effective normal stress; lab dry or wet; 20–100 °C) showed that the sandstone-derived gouges are characterised by virtually normal stress- and temperature-independent friction coefficients ($\mu \approx 0.5$–0.6). The data exhibited stable, velocity-strengthening behaviour moving towards near-neutral velocity-dependent behaviour with increasing effective normal stress. The carbonate-rich fault rock gouges exhibited higher friction coefficients ($\mu \approx 0.6$–0.7), with a transition from velocity-strengthening behaviour at room temperature (dry) to velocity-weakening behaviour at 100 °C (dry and wet), i.e. a transition from stable sliding to potentially unstable or seismogenic slip. Cross-fault permeability decreased up to 1.5 orders with increasing displacement, showing slightly lower values for the carbonate-rich gouges. We infer that the mechanical behaviour of fault gouges derived from the sandstones studied will not be strongly influenced by long-term CO_2-exposure, due to the low content of reactive minerals in the protolith. Significant changes in frictional strength or (micro)seismic potential of faults present in a CO_2 storage system are only expected when there is major carbonate precipitation in the fault damage zone due to rapid CO_2 leakage and degassing.

1. Introduction

Carbon Capture and Storage (CCS) remains one of the few options for reducing CO_2 emissions while fossil fuels dominate the global energy mix. CCS entails carbon capture at point sources, followed by transport to and injection into geological formations (Benson et al., 2005; Haszeldine, 2009), such as saline aquifers (Bachu et al., 1994; Gunter et al., 1997; Hitchon, 1996) or depleted natural oil and gas reservoirs (Holloway, 2001). The latter are particularly attractive, as the reservoir structure is generally well-known and has proven capability of structurally trapping hydrocarbons for time-scales greater than ~100 years (Haszeldine et al., 2005). Oil and gas fields also possess the infrastructure needed to transport and inject large volumes of fluids. Moreover, CO_2 injection has been used for decades for enhanced oil and gas recovery (EOR: Gozalpour et al., 2005; EGR: Van der Meer et al., 2006), and is therefore not a radically new concept (Baines and Worden, 2004). Last but not least, long-term structural trapping of CO_2 in reservoir formations is not only an engineering concept, but also a natural phenomenon observed in numerous CO_2-charged reservoirs globally (Kampman et al., 2016; Pauwels et al., 2007; Pearce et al., 2004).

To ensure safe, long-term subsurface storage of anthropogenic CO_2, it is important to maintain sealing integrity of the reservoir-caprock system, and of faults therein, during and after CO_2 injection (e.g. Hawkes et al., 2005; Kampman et al., 2016). In addition to a direct poro-elastic response of the reservoir to the increase in pore pressure (Wang, 2000), it is well established that, unlike methane, reaction with injected CO_2 can result in a range of chemically coupled mechanical (Hangx et al., 2013, 2010a; Le Guen et al., 2007; Liteanu and Spiers, 2009; Liteanu et al., 2013; Major et al., 2014; Mikhaltsevitch et al., 2014) and/or hydrological effects (Huq et al., 2015; Lamy-Chappuis et al., 2014; Luquot and Gouze, 2009; Smith

* Corresponding author.
E-mail address: E.Bakker1@uu.nl (E. Bakker).
[1] Current address: High Pressure and Temperature Laboratory, Utrecht University, The Netherlands.

http://dx.doi.org/10.1016/j.ijggc.2016.08.029
1750-5836/

et al., 2013; Vialle et al., 2014; Vialle and Vanorio, 2011). In general, CO_2 will dissolve in the formation brine, forming carbonic acid thus releasing H^+ and inducing chemical interaction with the host rock (Bachu et al., 1994). However, CO_2-brine-rock interactions are very slow and strongly depend on the availability of reactive minerals (Bachu et al., 1994; Baines and Worden, 2004). The long time-scales and the complexity of brine-rock systems make it difficult to reproduce these processes in geomechanical experiments. For this reason, most experimental studies of chemical/mechanical interactions have focused on the effects of relatively rapid, short-term CO_2-brine-rock interactions on the mechanical behaviour of intact reservoir rocks and caprocks (Hangx et al., 2013; Le Guen et al., 2007; Liteanu et al., 2013; Major et al., 2014; Mikhaltsevitch et al., 2014; Vialle and Vanorio, 2011), and of faults and fractures (Edlmann et al., 2013; Pluymakers et al., 2014; Samuelson and Spiers, 2012).

In order to investigate the effects of long-term CO_2-brine-rock interactions on reservoir and caprock properties, an alternative approach is to study samples recovered from natural CO_2 fields. Well-known examples of clastic CO_2 fields include the Werkendam field, near Rotterdam, the Netherlands (Hangx et al., 2015), the Brae and Miller fields, in the UK section of the North Sea (Haszeldine et al., 2005), the fields close to Green River in the Colorado Plateau, USA (Kampman et al., 2016; Pearce et al., 2004), and the Otway Basin fields of Australia (Watson et al., 2003). These fields are charged naturally with high concentrations of CO_2 and have experienced CO_2-brine-rock interactions over geological time-scales. Comparison of rocks exposed to CO_2 from such fields with laterally equivalent but unexposed material offers an opportunity to better understand the long-term effects of CO_2 on rock composition and properties, thus aiding the assessment of risks related to CO_2 storage. Such studies have focused on the mineralogical, geochemical and diagenetic effects of long-term CO_2-exposure (Kampman et al., 2016; Watson et al., 2003), with only a few studies investigating the coupled effect of CO_2-brine-rock interactions on the mechanical and/or transport properties of reservoir rocks and caprocks (Busch et al., 2014; Hangx et al., 2015). Even fewer studies have been published on the effects of long-term CO_2-brine-rock interaction on the properties of fault rocks (Hangx et al., 2015; Trippetta et al., 2013). Within a CO_2 storage system, faults that either cross-cut or bound the reservoir offer a variety of potential leakage risks (White and Foxall, 2016). For example, in response to stress changes resulting from CO_2 injection, faults may be reactivated, with internal damage enhancing leakage path potential. Moreover, long-term CO_2-induced changes in mineralogical composition and porosity may influence fault integrity directly or may promote fault slip by changing fault frictional behaviour, slip stability and hence transport properties (Hangx et al., 2015; Samuelson and Spiers, 2012; Trippetta et al., 2013). It is well established that mineral composition strongly influences fault frictional properties (e.g. Moore and Lockner, 2004; Tembe et al., 2010). However, effects of long-term CO_2-brine-rock interactions on the mineralogical, frictional and transport properties of fault rock have not been specifically studied to date.

In an attempt to help fill this knowledge gap, we performed direct shear experiments aimed at assessing the long-term effect of CO_2-brine-rock interactions and resulting mineralogical changes on the frictional strength, slip stability (seismogenic potential), and permeability of simulated fault gouges prepared from samples of the Entrada Sandstone formation, taken from a natural CO_2 reservoir located in the Paradox Basin in the Green River region of the Colorado Plateau, SE Utah, USA (in this study referred to as the Green River reservoir). These simulated gouges consisted of finely powdered host rock material, as opposed to natural fault gouge. The gouges were prepared from intact unexposed (unreacted) and a CO_2-exposed (reacted) quartz-rich, Entrada Sandstone reservoir rock, as well as from carbonate-cemented fault rock taken from the Salt Wash Fault (SWF) at a point where this fault, which is an active conduit for leaking CO_2, cuts the Entrada Sandstone. It should be noted that comparative studies have shown that the microstructures and frictional behaviour of natural gouges can be simulated realistically using this method (for example see Rutter et al., 1986; Haines et al., 2009; Delle Piane et al., in press). The experiments were performed under in-situ reservoir conditions relevant for CCS projects, i.e. at temperatures of 20 and 100 °C, effective normal stresses (σ_n^{eff}) in the range 5–90 MPa, both dry and in the presence of an aqueous pore fluid (pore pressure P_f = 25 MPa). Direct shearing velocities of 0.22–10.86 μm/s were used. We discuss how differences in mineralogical composition due to CO_2-exposure, superimposed on primary lithological variation, affect fault rock properties and the implications that this has for long-term CO_2 storage.

2. Geological setting and starting material

2.1. Geological setting of the Entrada Sandstone

The Entrada Sandstone starting material was collected near Tenmile Butt, from surface exposures located close to and within, the Salt Wash Fault zone, in the northern part of the Paradox Basin, SE Utah, USA (see Fig. 1). The material was provided courtesy of Dr. Niko Kampman (Shell Global Solutions).

The extent of the Paradox Basin is defined as the area of salt deposition in the Middle Pennsylvanian Paradox Formation. To the north-west and north, the basin is bounded by the San Rafael Swell and Uncompahgre Plateau, while the east and south-east ends of the basin are defined by the San Juan Dome and Hogback Monocline (see Fig. 1A) (Nuccio and Condon, 1996). Sediment deposition occurred in a half-graben structure adjacent to the SW-bounding faults of the Pennsylvanian Uncompahgre uplift, which supplied arkosic debris to the northern margin of the basin (Baars and Stevenson, 1981). Basin filling consists of a sequence of Palaeozoic marine sediments overlain by Triassic and Jurassic mainly alluvial sediments, including alternating sequences of low conductivity silts and mudstones (aquitards) and hydraulically conductive, predominantly aeolian sediments, such as the Jurassic Entrada Sandstone (Fig. 1B).

During the Cretaceous, diapiric rise of thick Carboniferous evaporites and movement along pre-existing faults in the Precambrian basement resulted in the formation of NW-SE-trending faults, anticlines and synclines, the so-called Paradox Fold and Fault belt (Fig. 1A), in the northern part of the basin (Baars and Stevenson, 1981; Nuccio and Condon, 1996). Though the timing is poorly constrained, it has been postulated that reactivation of these fold and fault structures occurred during the Laramide orogeny (Baars and Stevenson, 1981; Shipton et al., 2004).

The north-plunging Green River anticline is cut by two east-west trending normal faults: the Little Grand Wash Fault (LGWF) and the Salt Wash Fault (SWF). At the crest of the anticline, beneath the south-dipping faults, CO_2 has accumulated. The CO_2 was sourced by clay-carbonate reactions in underlying limestones of the Paradox Formation (Shipton et al., 2004), possibly supplemented by a magmatic source (Wilkinson et al., 2008). Leakage of subsurface CO_2 along the LGWF and SWF commenced approximately 100–400 ka ago (Burnside et al., 2013), leading to CO_2-induced reactions in the corresponding fault cores and adjacent damage zones, such as seen in the Entrada Sandstone (Kampman et al., 2014; Shipton et al., 2004).

The Entrada Sandstone unit is a ~150–450 m thick (Ogata et al., 2014), reddish sandstone, which crops out as shown in Fig. 1B. It consists mainly of quartz and feldspar and is cemented

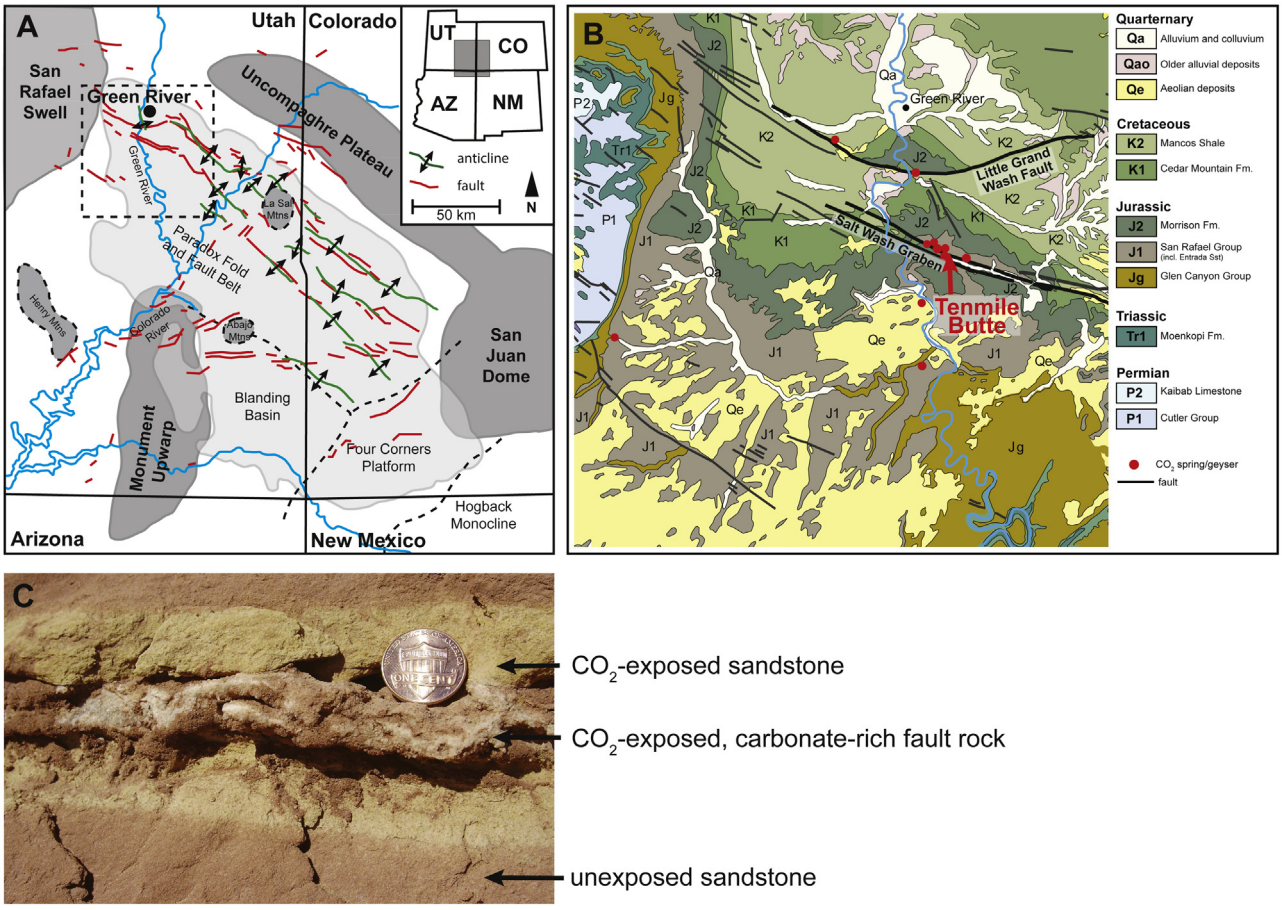

Fig. 1. Sampling location in the Green River Field, Paradox basin, Utah, USA. A) Map illustrating the main anticlinal structures, faults and structural provinces of the Paradox Basin and adjacent areas. Dashed lines indicate transitional or indefinite boundaries between elements (after Condon, 1997). B) Geological map of area near the Salt Wash Graben and Little Grand Wash Fault (location inset Fig. 1A) showing the position of the sampling location at Tenmile Butte (after Hintze et al., 2000). C) Photograph of the Entrada Sandstone showing a CO_2-exposed fault zone cutting the virgin (red, unexposed) sandstone (courtesy of Dr. N. Kampman). Note the bleached, CO_2-exposed sandstone at the margins of the fault zone. (For interpretation of the references to colour in this figure legend, the reader is referred to the web version of this article.)

predominantly by quartz, dolomite and calcite (Wigley et al., 2012). The Entrada sandstone is therefore lithologically similar, in broad terms, to many natural gas reservoirs around the world (Shipton et al., 2004). Locally, however, it contains bleached zones that consist of reduced amounts of quartz and feldspar with calcite and dolomite cement filling the pores (Wigley et al., 2012). In the case of the SWF, CO_2 leakage has led to extensive carbonate precipitation, where it traverses the Entrada Sandstones (Burnside et al., 2013).

2.2. Sample material

The Entrada Sandstone and fault rock material used in this study was taken from three nearby outcrops at Tenmile Butt (Fig. 1B), in the Green River field, showing varying degrees of CO_2-exposure: 1) red-coloured, unreacted and mechanically intact reservoir material, referred to here as 'unexposed sandstone', 2) pale yellow-coloured, mechanically intact reservoir rock exposed to CO_2-rich fluid, i.e. 'CO_2-exposed sandstone', and 3) white-coloured fault rock obtained from the footwall of the actively CO_2-leaking SWF, referred to as 'CO_2-exposed, carbonate-rich fault rock' (Fig. 1C).

Each of these materials was characterised using optical microscopy and X-ray diffraction (XRD) analysis (see Table 1). The red, unexposed sandstone samples consisted mainly of quartz (60–70%), feldspar (11–15%, occasionally up to ~20%) and minor amounts of phyllosilicates (muscovite; 6–9%). The grains are angular to rounded (grain size: ~100 μm), locally indented by pressure solution, and cemented by predominantly dolomite and calcite (3–10%), resulting in ~10% porosity. Moreover, minor amounts of hematite (~0.40%) were detected, being optically visible as grain coatings and giving the rock its characteristic reddish colour. The bleached, CO_2-exposed sandstone samples consisted of increased amounts of quartz (75–90%) and mostly lower amounts of feldspar (3–5%, occasionally ~20%), phyllosilicate (muscovite; 2–3.5%), carbonates (calcite plus dolomite: 1.5–3.0%) and hematite (<0.5%), in rough accordance with expectations for reaction of the red protolith with CO_2 (Wigley et al., 2012). The grains in this material are a little more angular (grain size: ~125 μm), with some grains showing irregular boundaries, suggesting corrosion due to dissolution. Cement is predominantly formed by large, irregularly shaped patches of quartz-cement (250–300 μm), with clearly less carbonate. The porosity of the bleached samples is 5–10%. Cemented fault rock sampled from the SWF consisted of veins containing large (1 cm) spheroidal aggregates of radiating acicular aragonite (27–51%), plus minor amounts of calcite and dolomite (0.6–11%), embedded in a fine-grained sandstone matrix consisting of quartz (31–72%) with minor amounts of feldspar (5%) and phyllosilicates (muscovite; 5–19%). Locally, traces of hematite were detected. Simulated fault gouges were prepared from these three materials by crushing cm-sized samples using a mortar and pestle. The material was further crushed using a ball-mill until it attained a grain size that passed through a 35 μm sieve, representing the typical grain

Table 1
XRD data for the simulated gouges derived from the unexposed and CO_2-exposed reservoir rock, and the CO_2-exposed, carbonate-rich fault rock samples.

Mineral (mass-%)	Unexposed sandstone	CO_2-exposed sandstone	CO_2-exposed fault rock
quartz	58.8–70.5	75.9–90.5	31.1–71.5
calcite	2.1–5.9	<1.2	0.6–7.2
dolomite	1.1–4.7	1.0–2.2	<3.7
aragonite	n.d.	n.d.	26.7–40.0
albite	<6.6 (occasionally 19.7)	n.d.	n.d.
microcline	9.9–13.3	3.1–5.4 (occasionally 19.8)	n.d.
bytownite	n.d.	n.d.	<5.0
dickite	<2.1	n.d.	n.d.
phyllosilicate (muscovite)	4.2–8.9	1.9–3.4	4.8–18.0
hematite	0.4	<0.5	<1.5
magnetite	n.d.	<1.0	n.d.

Note: 'n.d.' indicates that the corresponding phase is below the detection limit.

size range observed in simulated and natural fault gouges (Byerlee and Summers, 1976; Keulen et al., 2007).

3. Experimental aspects

A total of 23 direct shear experiments were conducted to investigate the effects of effective normal stress (σ_n^{eff}), temperature (T) and pore fluid (added at pressure P_f) on the frictional properties of the three types of simulated fault gouge samples described above. We performed four series of experiments on each of these three sample types:

1) Experiments at room temperature, under lab dry conditions (room humidity) and at σ_n^{eff} of 5–90 MPa (Data-set 1),
2) Experiments at elevated temperature (T = 100° C), under lab dry conditions and at σ_n^{eff} = 50 MPa (Data-set 2),
3) Experiments at elevated temperature (T = 100° C) employing an aqueous pore fluid at a pressure P_f = 25 MPa and at σ_n^{eff} = 50 MPa (Data-set 3),
4) Experiments performed on vacuum-dried samples at room temperature and at σ_n^{eff} = 50 MPa, using argon as the pore fluid (P_f = 2 MPa) and making argon permeability measurements before, during and after shear (Data-set 4).

Aqueous pore fluid solutions were prepared by adding excess amounts of fine-grained, crushed powder of the respective sample material to distilled water and stirring until used in the wet experiments (i.e. for at least 24 h). These solutions were assumed to be saturated with soluble components before use, thereby preventing dissolution of these components during our wet experiments. All experiments performed are summarised in Table 2.

3.1. Experimental procedure: direct shear experiments

Direct shear experiments were performed on the simulated fault gouges using a conventional triaxial compression machine (see Supplementary material, Fig. S1), equipped with a specially-designed direct shear assembly (Fig. S2—see also Samuelson and Spiers, 2012). The apparatus consists of an externally heated main pressure vessel, with silicone oil as the confining medium, linked to an auxiliary pressure-compensation vessel (Hangx et al., 2010b; Peach, 1991). Load is transmitted to the sample using a yoke/piston assembly, which is driven by a motor/gearbox/ball-screw system. Upon advancement of the piston, a shear stress is imposed on the gouge layer and sliding is initiated at a constant sliding velocity of 5 μm/s. To investigate the velocity-dependence of friction of the three types of simulated fault gouges a five-step velocity-stepping sequence is employed. The displacement velocity is determined by the gears of the motor driving the loading piston, being equivalent to sliding velocities of 0.22-1.086-10.86-1.086-0.22 μm/s.

During each shear experiment, internal axial load, piston displacement, confining pressure and sample temperature were logged every 2 s. The shear stress is equal to the internal axial load divided by the contact area of the shear surface, which is assumed to remain equal to the initial contact area. From the shear stress and the normal stress, the apparent coefficient of friction μ was calculated as $\mu = \tau/\sigma_n^{eff}$, in effect including any minor cohesion effects in μ (cf. den Hartog et al., 2013; Niemeijer and Vissers, 2014). For the sake of simplicity, we will refer to μ as the friction coefficient.

The slip rate-dependence of μ, obtained from the velocity-stepping shear experiments, was analysed using the rate and state friction (RSF) approach (Marone, 1998) and expressed in terms of (a–b) (see Supplementary material Section S1.4). In short, a positive (a–b)-value means the material exhibits 'velocity-strengthening' behaviour, implying that the system is inherently stable and that the accelerating slip needed for seismogenesis cannot occur (Scholz, 1998), at least within the RSF approach to quantifying friction. On the other hand, 'velocity-weakening' behaviour occurs if (a–b) is negative. In this case, the system is potentially unstable (Scholz, 1998), i.e. able to produce repetitive stick-slip events or seismogenic slip provided that the elastic stiffness of the loading system falls in the right range (e.g. Scholz, 2002). It should be noted that velocity step-related changes in friction coefficient are often superimposed onto a gradual increase or decrease of μ with increasing slip distance, a so-called slip-hardening or slip-softening trend, respectively. Slip-hardening is often associated with ongoing grain size reduction through cataclasis, whereas slip-softening is associated with ongoing localization of shear deformation (Kanagawa et al., 2000; Niemeijer et al., 2008). However, in our experimental configuration, slip-softening might be an artefact from a decreasing load-bearing area of contact.

3.2. Experimental procedure: permeability measurements

A total of three direct shear experiments coupled to 'cross-fault permeability' (κ) measurements were performed on dry samples, at room temperature, using argon gas permeametry. This method employed the decay of a 2 MPa argon gas pressure difference imposed suddenly across the sample (Sutherland and Cave, 1980)—see Supplementary material Section S2 for more details. Permeametry was carried out before, during and after shear using the same direct shear and velocity-stepping procedure as described above. The argon pressure signals measured at each end of the sample were logged and used to calculate cross-fault permeability by analysing the pressure decay using the method described by Sutherland and Cave (1980).

Table 2
Overview of the experiments performed in this study. Samples were tested lab dry, wet with a sample saturated-solution or using dry argon gas.

Expt.	Material	σ_n^{eff} (MPa)	V (μm/s)	μ_{final} (−)	Motion
Data-set 1: effect of effective normal stress, σ_n^{eff} (lab dry (room humidity), room temperature)					
Un01	unexposed sandstone	5	5.43-0.22-1.086-10.86-1.086-0.22	0.71	VS
Un02	unexposed sandstone	25	5.43-0.22-1.086-10.86-1.086-0.22	0.56	VS
Un03	unexposed sandstone	50	5.43-0.22-1.086-10.86-1.086-0.22	0.57	VS
Un04	unexposed sandstone	50	5.43-0.22-1.086-10.86-1.086-0.22	0.61	VS
Un05	unexposed sandstone	75	5.43-0.22-1.086-10.86-1.086-0.22	0.58	VS
Un06	unexposed sandstone	75	5.43-0.22-1.086-10.86-1.086-0.22	0.56	VS
Un07	unexposed sandstone	90	5.43-0.22-1.086-10.86-1.086-0.22	0.60	VS
Ex01	CO_2-exposed sandstone	5	5.43-0.22-1.086-10.86-1.086-0.22	0.71	VS
Ex02	CO_2-exposed sandstone	25	5.43-0.22-1.086-10.86-1.086-0.22	0.59	VS
Ex03	CO_2-exposed sandstone	50	5.43-0.22-1.086-10.86-1.086-0.22	0.53	VS
Ex04	CO_2-exposed sandstone	50	5.43-0.22-1.086-10.86-1.086-0.22	0.53	VS
Ex05	CO_2-exposed sandstone	75	5.43-0.22-1.086-10.86-1.086-0.22	0.61	VS
Ex06	CO_2-exposed sandstone	75	5.43-0.22-1.086-10.86-1.086-0.22	0.59	VS
Ex07	CO_2-exposed sandstone	90	5.43-0.22-1.086-10.86-1.086-0.22	0.62	VS
FR01	CO_2-exposed fault rock	5	5.43-0.22-1.086-10.86-1.086-0.22	0.82	VS
FR02	CO_2-exposed fault rock	5	5.43-0.22-1.086-10.86-1.086-0.22	0.92	VS
FR03	CO_2-exposed fault rock	5	5.43-0.22-1.086-10.86-1.086-0.22	0.89	VS
FR04	CO_2-exposed fault rock	25	5.43-0.22-1.086-10.86-1.086-0.22	0.57	VS
FR05	CO_2-exposed fault rock	50	5.43-0.22-1.086-10.86-1.086-0.22	0.65	VS
FR06	CO_2-exposed fault rock	50	5.43-0.22-1.086-10.86-1.086-0.22	0.66	VS
FR07	CO_2-exposed fault rock	75	5.43-0.22-1.086-10.86-1.086-0.22	0.60	VS
FR08	CO_2-exposed fault rock	75	5.43-0.22-1.086-10.86-1.086-0.22	0.63	VS
FR09	CO_2-exposed fault rock	90	5.43-0.22-1.086-10.86-1.086-0.22	0.60	VS
Data-set 2: effect of temperature (σ_n^{eff} = 50 MPa, lab dry (room humidity), T = 100 °C)					
Un09	unexposed sandstone	50	5.43-0.22-1.086-10.86-1.086-0.22	0.66	VS-VW
Ex09	CO_2-exposed sandstone	50	5.43-0.22-1.086-10.86-1.086-0.22	0.65	VS-VW
FR11	CO_2-exposed fault rock	50	5.43-0.22-1.086-10.86-1.086-0.22	0.61	VW
Data-set 3: effect of saturated-solution (σ_n^{eff} = 50 MPa, P_f = 25 MPa, T = 100 °C)					
Un10	unexposed sandstone	50	5.43-0.22-1.086-10.86-1.086-0.22	0.55	VS-VW
Ex10	CO_2-exposed sandstone	50	5.43-0.22-1.086-10.86-1.086-0.22	0.42	VS
FR12	CO_2-exposed fault rock	50	5.43-0.22-1.086-10.86-1.086-0.22	0.62	VW
Data-set 4: effect of shear on across-fault argon permeability (σ_n^{eff} = 50 MPa, P_f = 2 MPa, room temperature)					
Un08	unexposed sandstone	50	5.43-0.543 (3×)	0.47	–
Ex08	CO_2-exposed sandstone	50	5.43-0.543 (3×)	0.55	–
FR10	CO_2-exposed fault rock	50	5.43-0.543 (3×)	0.49	–

Symbols: σ_n^{eff} denotes effective normal stress, P_f denotes pore pressure, T denotes temperature, V denotes sliding velocity and μ_{final} denotes the friction coefficient measured at the end of each experiment (~5–7 mm displacement). Motion: 'VS' indicates that a sample exhibited velocity-strengthening slip behaviour, while 'VW' indicates velocity-weakening slip behaviour.

4. Results

In this paper, we adopt the convention that compressive stresses are positive. In our friction experiments, we take the yield point in the run-in stage of individual experiments as the point of maximum curvature of the friction coefficient vs. displacement curves. We take the effective normal stress (σ_n^{eff}) as the applied confining pressure hence normal stress (σ_n) minus the applied pore pressure (P_f), thus defining it as:

$$\sigma_n^{eff} = \sigma_n - P_f \quad (1)$$

4.1. Mechanical data

4.1.1. Frictional behaviour of dry gouges at room temperature (Data-set 1)

The evolution of the friction coefficient as a function of shear displacement is shown in Fig. 2A and B for representative subsets of experiments performed under lab dry conditions on all three sample types, at room temperature and at 5, 25, 50 and 90 MPa effective normal stress (Data-set 1). All μ vs. displacement curves obtained at room temperature in the present study are characterised by a near-linear increase in μ until yielding occurs. Yielding is observed at a shear displacement x of 0.4–0.6 mm and at a friction coefficient of ~0.55–0.75 at low σ_n^{eff} (5 MPa), versus 0.5–1.0 mm and $\mu \approx 0.55$ at intermediate to high σ_n^{eff} (25–90 MPa) (Fig. 2A and B). Yielding is usually followed by minor slip-hardening, reaching near steady-state friction values at a shear displacement x of ~1.6 mm. At this displacement, the first velocity step was applied. In subsequent velocity-stepping stages, similar velocity-strengthening (stable slip) frictional behaviour is observed for all three materials when performed at the same applied normal stress. The frictional response to upward velocity steps frequently lacks a distinct peak due to the absence of subsequent weakening (cf. compare Figs. 2 A and B and S3).

Though steady-state is approached in most tests shortly beyond yield, tests performed on all three sample materials at low normal stress (σ_n^{eff} = 5 MPa) show slip-hardening superimposed on the majority of subsequent velocity steps, resulting in relatively high friction coefficient values of ~0.70–0.90 in later stages of the experiments (Fig. 2A and B). The friction coefficient curves obtained at intermediate to high normal stress (σ_n^{eff} = 25–90 MPa) are characterised by zero to minor slip-hardening, and/or minor slip-softening towards higher displacements, superimposed onto a modest velocity-strengthening response to the applied velocity steps. This results in final friction coefficient values ranging between ~0.60 and 0.63 (see Fig. 2A and B). An exception is experiment EX03 (CO_2-exposed Entrada Sandstone, 50 MPa, Fig. 2B), which shows yielding behaviour similar to unexposed Entrada Sandstone (UN03) and CO_2-exposed, carbonate-rich fault (FR05) gouges, but with subsequent slip-softening upon velocity stepping, resulting in a final friction coefficient of only ~0.53.

The dependence of shear stress, supported both at yield and at maximum sliding velocity, on σ_n^{eff} is shown for all three sample

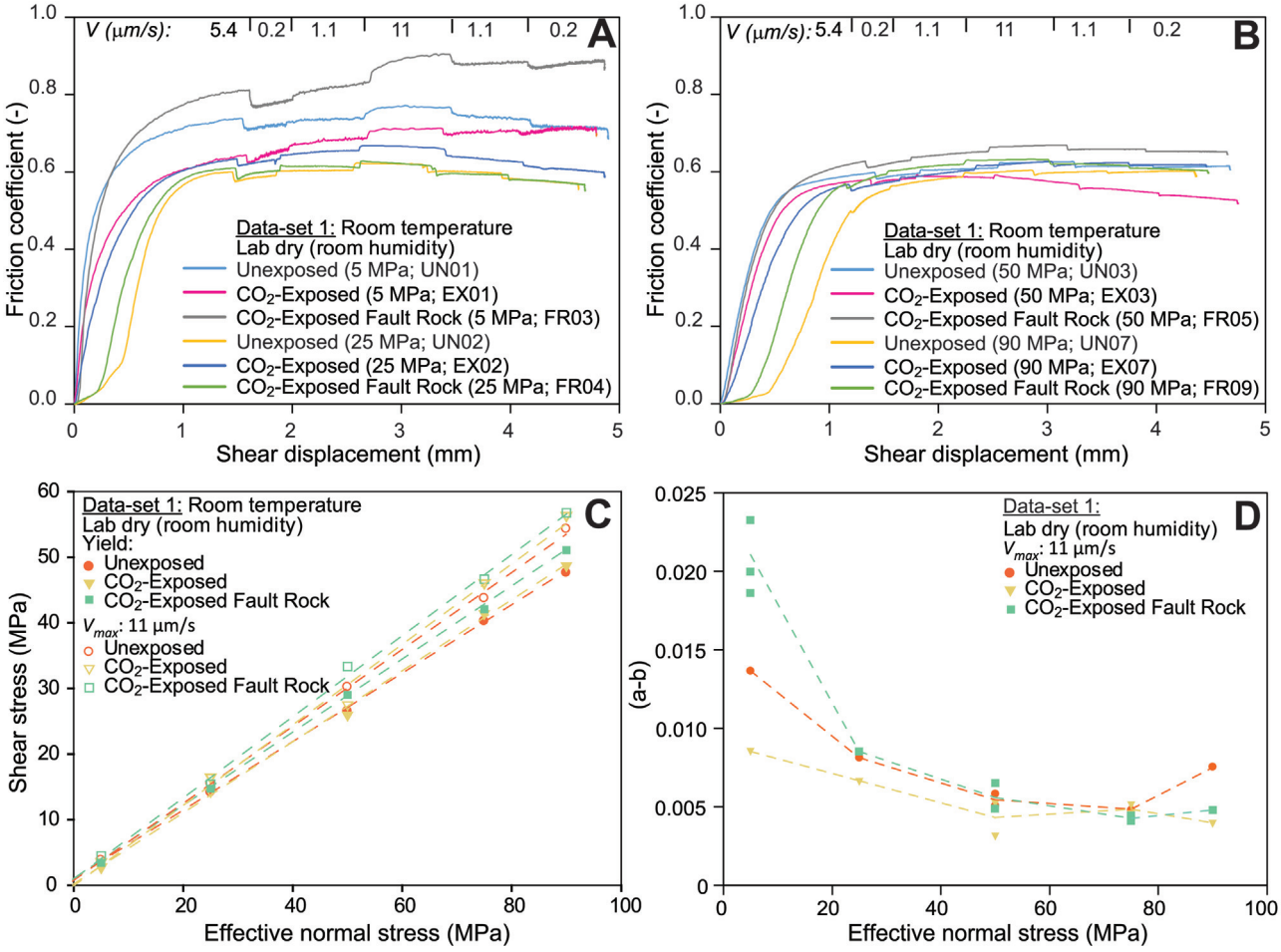

Fig. 2. Representative mechanical data for all sample types sheared under lab-dry conditions at room temperature (Data-set 1). A) Friction coefficient vs. shear displacement curves for velocity-stepping experiments conducted at normal stresses of 5 and 25 MPa using the velocity steps indicated at the top of the figure. B) Similar data for samples tested at normal stresses of 50–90 MPa. Note that samples tested at 25–90 MPa show similar behaviour. C) Shear stress at yield (solid symbols) and shear stress at maximum sliding velocity (open symbols) vs. the effective normal stress for experiments performed at room conditions. D) Velocity-dependence parameter (a–b) versus normal stress. All samples show a decrease in (a–b) with increasing effective normal stress, at least up to σ_n^{eff} = 75 MPa.

types deformed dry at room temperature in Fig. 2C. For all three materials, the data show a linear trend between shear and effective normal stress, which can be described by a Coulomb-type criterion given as:

$$\tau = \mu_i \sigma_n^{eff} + C_0 \quad (2)$$

where μ_i is the internal friction coefficient (i.e. the slope of the trend) and C_0 represents the cohesion of the simulated fault gouge (i.e. the intercept of the trend with the vertical axis). It should be noted that for granular materials, like fault gouge, cohesion is generally low, but not necessarily zero. Cohesion is in essence a measure for the extent to which grain-to-grain contacts present in the gouge material are actively experiencing frictional sliding or deformation during shear. In our experiments, the shear stress obtained at yield was used as a reference strength parameter, thus excluding any secondary effects of slip-hardening, when interpreting μ_i and C_0 values. At yield, linear least square fits to the data show that μ_i has values of 0.52 ± 0.011, 0.54 ± 0.017, 0.56 ± 0.007 and C_0 is of the order of 0.71 ± 0.64, 0.0 (zero) ± 1.0 and 0.73 ± 0.36 MPa, for unexposed sandstone, CO_2-exposed sandstone, and carbonate-rich fault rock gouges respectively. The linear relations describing the steady-state shear stress supported at maximum sliding velocity (V_{max} = 10.86 μm/s), show higher internal friction coefficients, 0.58 ± 0.017, 0.62 ± 0.03, 0.61 ± 0.014, and cohesion values, 0.89 ± 1.0, 0.0 (zero) ± 1.3, and 1.39 ± 0.76. Gouge cohesion is mainly a minor feature, as suggested by the cohesion values. In most cases, certainly in experiments performed at $\sigma_n^{eff} \geq 25$ MPa, the relative contribution of cohesion to μ is negligible, justifying the use of $\mu = \tau/\sigma_n^{eff}$ as a measure of frictional strength in our RSF analysis. However, cohesion is significant in the tests performed at σ_n^{eff} = 5 MPa, as reflected in the higher μ-values for these samples seen in Fig. 2A. Note, that the cohesion observed for the CO_2-exposed, carbonate-rich fault-derived gouge is consistently higher than observed for the unexposed as well as the CO_2-exposed reservoir rock gouges.

Focusing now on the friction coefficient values obtained at or near steady state (μ_{ss}) in the dry experiments at room temperature, it is evident from Fig. 2A and B that these values increase with sliding velocity, reaching maximum values at velocities of ~11 μm/s ranging from 0.63 to 0.67 at σ_n^{eff}-values of 25–90 MPa (for $x \approx 3.3$ mm) and from 0.71 to 0.91 at σ_n^{eff} = 5 MPa (for $x \approx 3.5$ mm). This is followed by a decrease in frictional strength upon decreasing sliding velocity. In general, the unexposed and CO_2-exposed sandstone gouges show slightly lower μ-values than the carbonate-rich fault gouges.

The (a–b)-values obtained for all three gouges under dry, room temperature conditions are all positive and overall very similar at $\sigma_n^{eff} \geq 25$ MPa. Representative data are shown in Fig. 2D. Although velocity down-steps were analysed and show similar (a–b)-values to up-steps, we focus on (a–b)-values obtained for the up-steps

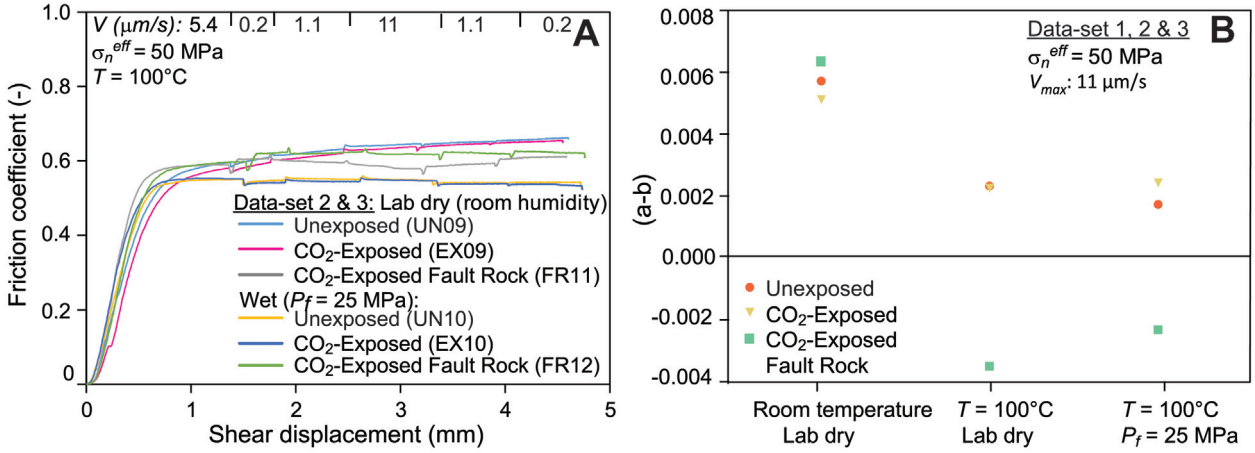

Fig. 3. Representative mechanical data for all sample types sheared under lab dry and wet conditions at room temperature and 100 °C (Data-set 1–3). A) Friction coefficient vs. displacement curves obtained from experiments conducted at elevated temperature, both dry and wet using the velocity steps indicated at the top. B) Velocity-dependence parameter (a–b) obtained for dry and wet samples at 100 °C, plus comparison with dry, room temperature data. Velocity-dependence is shown for a velocity step from ~1 to 11 μm/s, but similar values were obtained for all steps conducted. Only the carbonate-rich fault gouges show a tendency towards velocity-weakening behaviour.

as it is these that are relevant for earthquake nucleation. For readability we present only data for up-steps from 1 to 11 μm/s. The (a–b)-values obtained at σ_n^{eff} = 5 MPa are consistently higher (0.002–0.05) for all three sample types than those obtained at higher effective normal stresses (0.0007–0.01), especially for the fault rock-derived samples. CO_2-exposed Entrada Sandstone gouge generally shows slightly lower (a–b)-values, for the intermediate effective normal stresses, compared to the unexposed quartz-rich and CO_2-exposed, carbonate-rich fault rock. Though part of the data-set is not shown here for readability reasons, we note that (a–b) for all three gouges shows a rough tendency to increase with increasing post-step velocity for up-steps.

4.1.2. Frictional behaviour of dry and wet samples at 100 °C (Data-set 2 and 3)

Friction coefficient vs. displacement curves obtained at T = 100 °C and σ_n^{eff} = 50 MPa, for all three sample types under lab dry (Data-set 2) and solution-flooded (Data-set 3: P_f = 25 MPa) conditions are shown in Fig. 3A. As seen from this data, all three gouge types (unexposed sandstone (UN09), CO_2-exposed sandstone (EX09), and CO_2-exposed, carbonate-rich fault rock (FR11)) deformed dry at 100 °C exhibited closely similar initial behaviour, characterised by a near-linear increase in μ until apparent yielding at a friction coefficient of ~0.56–0.57 ($x \approx$ 0.7–0.9 mm—Fig. 3A), followed by minor slip-hardening. In the experiments on the dry, quartz-rich sandstone-derived gouges (UN09 and EX09), the friction coefficient increased from ~0.58, just beyond yield and prior to the first velocity-step, to ~0.65 at the end of the experiment. By contrast, the dry, carbonate-rich fault rock sample (FR11) displays slip-softening behaviour during the velocity up-steps, between a shear displacement of ~1.5 and 3.0 mm, followed by slip-hardening during the subsequent velocity down steps. Overall, the frictional strength of lab dry samples, at 100 °C and 50 MPa effective normal stress, is very similar to that seen in room temperature runs at the same conditions.

Compared with their dry equivalents, the wet, unexposed (UN10) and CO_2-exposed (EX10) sandstone-derived samples are characterised by a more rapid increase in μ until yield at a slightly lower friction coefficient ($\mu \approx$ 0.54 at $x \approx$ 0.66 mm). These samples exhibited steady-state sliding behaviour during the remainder of the experiments, characterised by a slightly lower frictional strength than dry samples (~0.55 vs. ~0.65, respectively). The wet, CO_2-exposed, carbonate-rich fault-derived sample (FR12) exhibited near steady-state slip behaviour reaching a μ-value of ~0.62, comparable to the behaviour under dry condition ($\mu \approx$ 0.61).

Turning to the velocity-dependence of friction at 100 °C, our data for dry samples derived from unexposed and CO_2-exposed sandstone (Data-set 2; UN09 and EX09) exhibit velocity-strengthening (stable slip) behaviour as illustrated by the positive (a–b)-values shown in Fig. 3B, with the values being very similar for both materials. By comparison, the (a–b)-values obtained for the sample prepared from carbonate-rich fault rock (Data-set 2; FR11) are strongly negative, i.e. exhibiting markedly velocity-weakening (unstable slip) behaviour. All three materials show much lower (a–b)-values than obtained at room temperature (Fig. 3B).

The presence of a pore fluid at 100 °C appears to have little to no effect on the velocity-dependence of friction for the unexposed and CO_2-exposed sandstone-derived gouges (UN10 and EX10), as the (a–b)-values are closely similar at ~+0.002 for both materials under dry and wet conditions (Fig. 3B). The (a–b)-values obtained for the samples derived from carbonate-rich fault rock (FR12) remain firmly negative in the wet condition, reflecting velocity-weakening behaviour (Fig. 3B).

4.2. Permeability data

Values of κ obtained from our permeametry measurements performed on all three materials at room temperature, are plotted as a function of shear displacement in Fig. 4, along with the friction coefficient measured during shearing (Data-set 4). Overall, the frictional behaviour observed during these experiments is very similar to that seen in all other dry tests on the same materials (cf. Fig. 2A and B). However, in contrast to the velocity-stepping tests on dry gouges, the present velocity-stepping plus slide-hold-slide experiments are dominated by slip-softening behaviour, reaching μ-values of ~0.50–0.55 for the samples prepared from unexposed and CO_2-exposed sandstone (UN08 and EX08), and 0.46 for the sample derived from CO_2-exposed, carbonate-rich fault rock (FR10), at the maximum displacements attained of ~7 mm. All three experiments show relatively distinct peak stresses upon re-shearing after a period of hold. For all samples it is evident from Fig. 4 that κ decreases with accumulated shear displacement. Initial values obtained prior to shearing (point 1—Fig. 4) vary between $1.5 \cdot 10^{-15}$ and $6.8 \cdot 10^{-17}$ m^2. These decrease by a factor of 10 for the sandstone-derived samples (unexposed and exposed) and a factor of around 2 for the carbonate-rich sample during the first stage of deformation at V = 5.4 μm/s. The permeability of all samples

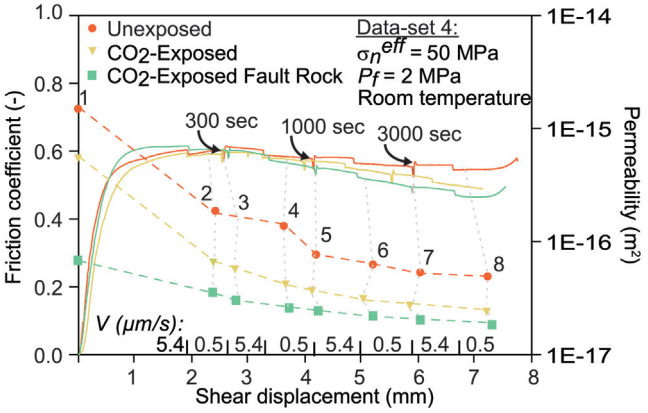

Fig. 4. Friction coefficient (solid lines) and gouge permeability (symbols) vs. shear displacement data obtained in the permeability experiments. Dashed tie-lines connect permeability measurements performed on the same samples. The experiments consisted of velocity-stepping tests combined with slide-hold-slide testing. Velocity-steps are shown. Hold periods are indicated with arrows. Permeability data points 2, 4 and 6 were determined during shear. Points 3, 5, 7 and 8 were measured during the hold periods shown.

continues to decrease with on-going shear displacement by a factor of 2 or 3. At the same time, κ-values measured during both shear and hold periods appear to lie on more or less the same κ-x trend-lines, suggesting little reduction in permeability during the hold periods. The final cross-fault argon permeability after ~7 mm of shear displacement (point 8), lies in the range of $5.0{\cdot}10^{-17}$ m^2 for unexposed sample material to $2.0{\cdot}10^{-17}$ m^2 for fault rock derived material.

5. Discussion

It has been widely suggested that geological storage of CO_2 can potentially lead to fault slip and induced seismicity via effects such as a reduction in effective normal stress and/or changes in the poro-elastic stress state of the storage reservoir, in response to an increase in pore pressure (e.g. Hawkes et al., 2005; Zoback and Gorelick, 2012). It has also been suggested that induced slip and seismicity can perhaps be promoted by a reduction in fault rock frictional strength and/or slip stability, i.e. a transition from positive to negative (a–b)-values, caused by CO_2-brine-rock interactions (Samuelson and Spiers, 2012). Critically, from the point of view of system integrity, induced fault slip may cause dilatation, subsequently increasing fault permeability. To help evaluate the slip, seismogenic and leakage potential of faults cutting clastic CO_2 reservoirs, we have investigated the frictional behaviour, slip stability and transport properties of simulated fault gouges derived from Entrada Sandstone samples taken from unexposed and CO_2-exposed portions of the formation at the Green River CO_2 reservoir site, and from the carbonate cemented material of the Salt Wash Fault, which is an active CO_2-leakage path.

In Europe, a significant number of recently investigated CCS pilot sites focus on sand and sandstone reservoir systems. Examples include the ROAD project (P-18 field, Triassic Bunter Sandstone; Dutch North Sea—Samuelson and Spiers, 2012), the (shelved) Peterhead CCS project (Goldeneye field, Lower Cretaceous Captain Sandstone; UK North Sea—Hangx et al., 2013), and the Sleipner CO_2 Storage project (Sleipner field, Miocene-Pliocene Utsira Sandstone; Norwegian North Sea—Chadwick et al., 2004). The Entrada Sandstone is considered a good analogue for many of these European sandstone reservoirs (Shipton et al., 2004), especially those that have a similar continental/aeolian origin, such as the Permian Rotliegend and Triassic Bunter gas reservoirs in the North Sea and onshore Netherlands regions. Accordingly, the long-term CO_2-charging of the Entrada Sandstone, and the effects of subsequent CO_2-induced mineral reactions superimposed on primary sediment and early diagenetic variability, offer a natural case-study for long-term CO_2 sequestration in sandstone reservoirs (Wigley et al., 2012).

Overall, our friction experiments on simulated fault gouges derived from naturally CO_2-exposed and unexposed Entrada Sandstone, are characterised by a friction coefficient ($\mu \approx 0.5$–0.6) that is virtually independent of normal stress and temperature, within the range of reservoir-relevant conditions investigated, i.e. 20–100 °C, $\sigma_n^{eff} \geq 25$ MPa (Fig. 2A and B). This range of conditions corresponds well with the temperatures and effective stresses expected in reservoir systems at depths up to ~3–4 km. The sandstone-derived gouges studied exhibit velocity-strengthening slip behaviour under all conditions studied (i.e. $(a-b) > 0$), with no significant effect of temperature on (a–b). However, keeping in mind reproducibility in the (a–b)-values (Niemeijer and Vissers, 2014), at room temperature they do show a slight decrease in (a–b) from velocity-strengthening at $\sigma_n^{eff} \leq 25$ MPa to near-neutral values at 75–90 MPa. Differences in mechanical behaviour between the CO_2-exposed and unexposed reservoir-derived gouges are clearly minor in our experiments (cf. Figs. 2 and 3), which is perhaps not surprising in view of the fact that the compositional differences are relatively minor. By contrast, the simulated gouges derived from the carbonate-rich fault rock exhibited higher friction coefficient values ($\mu \approx 0.6$–0.7) than the sandstones, though again these values were temperature-independent at $\sigma_n^{eff} \geq 25$ MPa. Interestingly, the (a–b)-data obtained for the carbonate-rich fault gouge showed a transition from velocity-strengthening behaviour at room temperature (dry) to velocity-weakening behaviour at 100 °C (both dry and wet), i.e. from stable sliding to unstable and potentially seismogenic slip. Finally, while the sandstone materials tested showed a decrease in cross-fault permeability with accumulated shear displacement by up to 1.5 orders of magnitude, i.e. from $\sim 10^{-15}$ m^2 in the undeformed state to $\sim 3.0{\cdot}10^{-17}$ m^2 at shear displacements of 6–7 mm, the carbonate-rich material showed a decrease only from $\sim 5.0{\cdot}10^{-17}$ m^2 to $2.0{\cdot}10^{-17}$ m^2 (cf. Fig. 4).

In the following, we discuss the effects of fault rock composition, normal stress, temperature, pore fluid and time on fault cohesion, frictional strength, slip stability, deformation mechanism and permeability evolution. This is done in the context of evaluating the effects of long-term exposure to CO_2 on fault rock behaviour and fault integrity during geological storage of CO_2 in sandstone reservoir rocks.

5.1. Contribution of cohesion to fault strength under laboratory vs. in-situ conditions

The gouge cohesion values obtained at yield in the present experiments, for the unexposed and CO_2-exposed quartz-rich sandstone and for the carbonate-rich fault rock, are respectively 0.71 ± 0.64, 0.0 (zero) ± 1.0 and 0.73 ± 0.36 MPa. This implies maximum cohesion values at yield of less than 1.5 MPa at our initial sliding velocity of 5.43 μm/s. For steady-state shearing at maximum sliding velocity ($V \approx 11$ μm/s), the corresponding cohesion values are slightly higher, specifically 0.89 ± 1.0, 0.0 (zero) ± 1.3, and 1.39 ± 0.76, implying maximum values around 2 MPa. Though gouge cohesion is minor, its relative contribution to the friction coefficient may be significant when the stresses acting on the fault plane are small, i.e. when C_0 is of the same order of magnitude as τ and σ_n^{eff} (cf. Eq. (2)). Compared with the shear stresses of 30–55 MPa supported by our samples at $\sigma_n^{eff} > 50$ MPa, cohesion values of 1–2 MPa are negligible, so that fault rock shear strength can be represented simply taking the ratio of shear stress over effective normal stress as the friction coefficient. However, for the experiments performed at normal stresses between 5 and 25 MPa,

a sample cohesion of ~1 MPa means that using $\mu = \tau/\sigma_n^{eff}$, leads to an underestimation of the shear strength that a fault can support by respectively 41 and 5%. In the case of real, reservoir-cutting faults that have been inactive over geological time, or have suffered only minor slip during hydrocarbons production, healing and cementation processes may lead to much higher cohesion (Tenthorey and Cox, 2006). The implication is that in establishing static failure criteria for faults in CO_2 storage systems where the effective pressure is expected to fall to say 25 MPa or less, cohesion cannot be neglected. Taking into account cohesion means injection pressure, and hence storage capacity, can be estimated higher than expected from purely frictional behaviour.

5.2. Effects of compositional differences and deformation conditions on the frictional behaviour of sandstone-derived gouges

Entrada Sandstone that has not been exposed to CO_2 consists predominantly of quartz and feldspar, with smaller amounts of phyllosilicates, carbonate cement and hematite (see Table 1). The hematite, which is present as grain-coatings, imparts the characteristic reddish colour to the unaltered sandstone. As described by Ogata et al. (2014), CO_2-induced alterations of the Entrada sandstone result in 'bleaching' or discolouration of the rock from red to pale yellow, through the dissolution of hematite. This is visible in our CO_2-exposed samples from the absence of hematite in most XRD data (Table 1). These samples also contain larger amounts of quartz, either as grains or inter-granular cement, and smaller amounts of feldspar, phyllosilicates and carbonates (Table 1). So, overall, an increase in quartz and a change in feldspar, carbonate and hematite content has been observed. These mineralogical changes are in agreement with the following geochemical reactions expected for CO_2 reacting with this type of sandstone:

Albite : $NaAlSi_3O_{8(s)} + H^+_{(aq)} + 4.5H_2O_{(l)} 4{\cdot}5H_2O_{(l)} \rightleftharpoons Na^+_{(aq)} + 2H_4\ SiO_{4(aq)} + 0.5Al_2Si_2O_5 0{\cdot}5Al_2Si_2O_5\ (OH)_{4(s)}$ (Stumm and Morgan, 1981)

Calcite : $CaCO_{3(s)} \rightleftharpoons Ca^{2+}_{(aq)} + CO_3{}^{2+}_{(aq)}$ (Stumm and Morgan, 1981)

Hematite : $Fe_2O_{3(s)} + 2CO_{2(g)} + SO_{2(g)} + H_2O_{(l)} \rightleftharpoons 2FeCO_{3(s)} + H_2SO_{4(aq)}$ (Palandri and Kharaka, 2005)

Muscovite : $KAl_2Si_3AlO_{10}{\cdot}(OH)_{2(s)} + 10H^+_{(aq)} \rightleftharpoons K^+_{(aq)} + 3Al^{3+}_{(aq)} + 3Si(OH)_{4(aq)}$ (Knauss and Wolery, 1989)

Weighed overall, our analyses of CO_2-exposed Entrada material, along with optical observations of grain surface corrosion and quartz cementation, suggest CO_2-related dissolution of feldspar, phyllosilicates and carbonate minerals plus precipitation of quartz (Table 1). Taking into account the composition of the unaltered samples, however, these inferred CO_2-related changes are most likely superimposed on local variations in mineralogy due to depositional fluctuations (Wigley et al., 2013) and early diagenetic variability.

In the present experiments, the unexposed and CO_2-exposed sandstone gouges exhibited closely similar frictional behaviour under dry conditions at room temperature (Fig. 2A and B), and under dry and wet conditions at elevated temperature (Fig. 3A). This behaviour is in good agreement with that observed in experiments on pure quartz and pure feldspar gouges (Mair and Marone, 1999; Morrow et al., 2000; Scruggs and Tullis, 1998; Shimamoto and Logan, 1981), as well as in experiments on simulated gouge prepared from gas reservoir sandstones (Hangx et al., 2015; Samuelson and Spiers, 2012), which generally show friction coefficients in the range 0.5–0.7, when tested dry and wet, at comparable conditions.

The slightly lower frictional strength exhibited by both our wet reservoir rock gouges (Fig. 3A) compared to the dry gouges (Fig. 2A and B) is also in agreement with the effect of water on pure quartz gouge prepared by Chester (1994). Furthermore, the observed slip-hardening behaviour seen under dry conditions is similar to that reported in other studies (Chester, 1994; Samuelson and Spiers, 2012; Tembe et al., 2010). This has previously been suggested to reflect cataclastic processes such as microcracking and comminution of the quartz grains, resulting in progressive compaction and thus strengthening of the gouge (Kanagawa et al., 2000; Niemeijer et al., 2008). Other clastic particles present in the gouge, such as feldspar and calcite, are expected to be affected by similar processes. Note that simulated gouges prepared from exposed and unexposed Entrada Sandstone samples show slip-neutral or truly steady-state sliding behaviour when sheared wet. This may be due to enhanced stress-corrosion cracking in the presence of water, allowing more rapid comminution and hence compaction in the initial stages of deformation, rendering a more mature and dense gouge, which is less prone to displacement-dependent evolution in the later stages of deformation.

Focusing now on the velocity-dependence of friction, gouge samples prepared from both unexposed and CO_2-exposed reservoir rock consistently showed velocity-strengthening behaviour at all conditions investigated. This agrees well with results obtained previously for pure quartz, pure feldspar, and natural sandstone gouges tested under similar experimental conditions (Chester, 1994; Hangx et al., 2015; Morrow et al., 2000; Samuelson and Spiers, 2012; Scruggs and Tullis, 1998; Shimamoto and Logan, 1981). Although slightly more marked, the observed decrease in $(a–b)$ with increasing normal stress seen in our room temperature experiments agrees well with that observed for pure quartz gouges (Mair and Marone, 1999). This decrease in $(a–b)$ is attributed to the decreasing effect of cohesion with increasing normal stress. Additionally, our $(a–b)$-values for lab dry samples show a decrease with temperature, between room temperature and 100 °C (Fig. 3B). Plotting our $(a–b)$ data for lab dry and fluid-saturated samples together with data for pure quartz gouges (Chester, 1994) shows that all data sets show a roughly similar trend, i.e. a decrease in $(a–b)$ with temperature, suggesting that temperature is important when evaluating the stability of a quartz-rich gouge (Fig. 5A).

Except for the tests performed at low effective normal stress (σ_n^{eff} = 5 MPa), where processes such as grain rolling/sliding may dominate deformation (Mair and Marone, 2001), we assume cataclasis plus granular flow to be the main mechanisms controlling deformation at room temperature. At the same time, however, the transition from velocity-strengthening to near velocity-neutral behaviour seen between ~20 and 100 °C (cf. Figs. 3 B and 5) suggests the activation of a temperature-dependent deformation process. Intracrystalline plasticity in quartz seems highly unlikely at such low temperatures, as it would occur at a vanishingly low rate (e.g. Hirth et al., 2001). However, in both wet and lab dry samples fluid-assisted processes such as pressure solution or subcritical crack growth are a possibility (Chester, 1994), recognizing that the lab dry (room humidity) samples must contain some water. In the case of a temperature-dependent, fluid-assisted process, such as pressure solution or subcritical crack growth, a clear effect of the addition of an aqueous pore fluid phase to dry samples might be expected to have a clear influence on strength and hence on $(a–b)$.

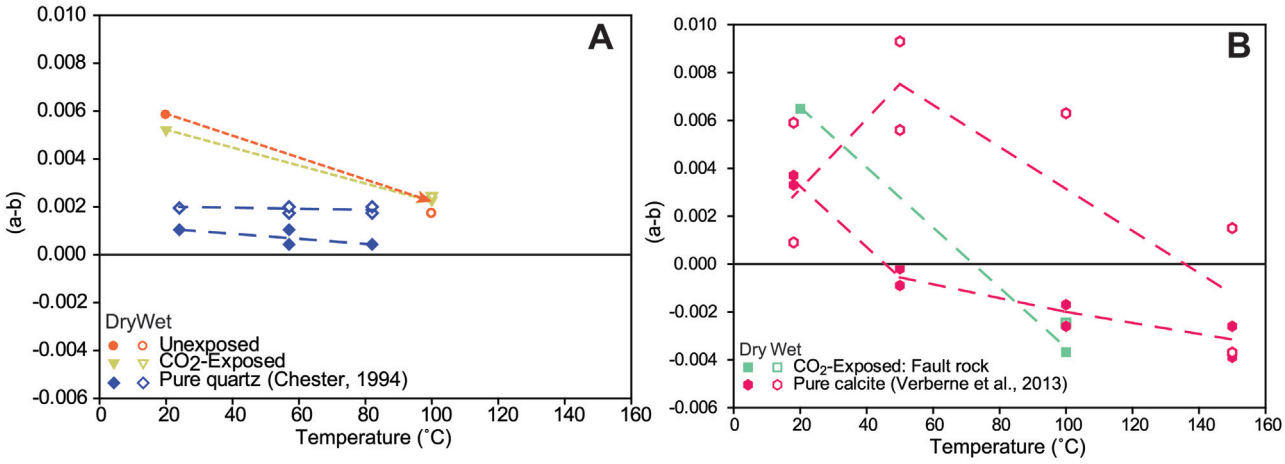

Fig. 5. Comparison of the velocity-dependence parameter (a–b) vs. temperature data for present samples with literature data. A) (a–b) vs. temperature data for the unexposed and CO_2-exposed Entrada Sandstone gouges plus literature data on pure quartz (Chester, 1994). B) (a–b) vs. temperature data for CO_2-exposed fault rock plus previous data on pure calcite (Verberne et al., 2014b). Solid symbols represent room dry experiments, open symbols represent solution-flooded samples. Note that the method applied by Chester (1994) to determine (a–b)-values consisted of fitting a single (a–b) value to two consecutive velocity-steps, plus a temperature-step.

No such effects were seen in our experiments (see Figs. 2 A and B and 3). However, we cannot exclude an effect of water on the velocity-dependence of the lab dry Entrada Sandstone gouges, as at room humidity sufficient moisture might still be present to allow fluid-assisted processes.

In conclusion, the detailed mechanisms dominating the frictional behaviour of our sandstone-derived gouges remain unclear. However, our observations do demonstrate that the mechanical behaviour of fault gouges derived from quartz-rich reservoir sandstones, similar to the Entrada Sandstone, will not be strongly influenced by long-term CO_2-exposure. In the present samples, this is undoubtedly because of the minor mineralogical impact of exposure to CO_2, i.e. due to the lack of sufficiently reactive minerals present in the host rock. On this basis, we can say that CO_2-brine-rock interactions are not expected to lead to significant changes in frictional strength or in (micro)seismic potential of faults present in a CO_2 storage system, as long as the fault rock composition is dominated by minerals such as quartz, along with subordinate amounts of K-feldspar and albite.

5.3. *Effects of carbonate precipitation on fault frictional behaviour*

In the Green River area of the Colorado Plateau (UT, USA), CO_2-charged springs occur along the Little Grand Wash Fault and the Salt Wash Fault. Here, and at a number of poorly abandoned wellbores, CO_2-charged water, saturated with respect to calcite, aragonite, dolomite and hematite leached from formations below the Entrada, leaks to the surface (e.g. see Kampman et al., 2016). As a result, multiple localised episodes of CO_2-degassing have led to extensive precipitation of aragonite, seen as cement within the leaking faults and surrounding damage zone, as well as in the form of travertine mounds at the surface, some of which date back 400 ka (Burnside et al., 2013). The SWF accordingly provides an interesting case-study for the loss of sealing integrity of a fault cross-cutting a CO_2-filled reservoir.

As shown in Table 1, material taken from a carbonate-filled section of the damage zone of the SWF consists of roughly equal amounts (~40 wt%) of quartz and aragonite, along with smaller amounts of calcite, dolomite, muscovite and hematite. It is not clear why aragonite preferentially precipitated over calcite, which is the more stable and less soluble polymorph of calcium carbonate (Langerak et al., 1999). Possible explanations lie in the faster precipitation kinetics of aragonite (e.g. Burton and Walter, 1987), together with the high supersaturation of the degassing fluid and high concentrations of Mg^{2+} and Fe^{2+} (Kampman et al., 2014), which inhibit calcite precipitation (e.g. Burton and Walter, 1987; Herzog et al., 1989).

As far as we are aware, no previous data exist on the frictional behaviour of aragonite-rich gouge materials, such as that investigated here. The present data therefore provide a new and useful contribution to understanding the frictional behaviour of faults in CO_2 storage systems that became cemented with aragonite due to leakage of CO_2-charged, Ca-saturated fluids (cf. the SWF). At room temperature conditions, the frictional strength of the fault samples that we have tested is similar to that of the quartz-dominated, sandstone-derived gouges (see Fig. 2A and B). The friction coefficient of 0.57–0.66 displayed by the dry, carbonate-rich samples is intermediate between that of simulated quartz (μ = 0.5–0.7) and calcite gouges (μ = 0.6–0.8) (Carpenter et al., 2016; Morrow et al., 2000; Shimamoto and Logan, 1981; Verberne et al., 2014b), and very similar to the values obtained for our unexposed and CO_2-exposed quartz-dominated samples. At 100 °C, both dry and wet samples of the carbonate-rich fault material showed frictional behaviour similar to that of pure calcite, as evidenced by a slight decrease in frictional strength, in agreement with experiments on calcite gouges (Verberne et al., 2014b).

In terms of (a–b)-values, dry, aragonite-rich fault samples deformed at room temperature showed stable, velocity-strengthening behaviour, in agreement with results for quartz-rich gouges (Chester, 1994; Samuelson and Spiers, 2012), and for calcite gouges (Verberne et al., 2014b). This presumably reflects cataclastic deformation plus granular flow. The observed decrease in (a–b) with increasing normal stress, also seen in the quartz-dominated gouge, is again attributed to the decreasing contribution of cohesion with increasing normal stress. By contrast, at 100 °C, both dry and wet carbonate-rich sample material consistently showed unstable, velocity-weakening behaviour (Fig. 3B). This is comparable to results obtained for pure calcite gouges which exhibit a transition from velocity-strengthening to velocity-weakening behaviour at temperatures above about 80 °C, as seen in Fig. 5B (Verberne et al., 2014b). By analogy with observations on lab dry and wet calcite (Verberne et al., 2014a,b), the transition from velocity-strengthening behaviour at room temperature to velocity-weakening behaviour at 100 °C seen in our carbonate-rich gouge samples is cautiously inferred to reflect an increase in

the importance of time-dependent, thermally-activated plastic or else water-assisted diffusive deformation of aragonite grains. Some support for crystal plasticity can be found in previous experiments on aragonite crystals that have demonstrated the operation of such deformation mechanisms at room temperature (e.g. Kearney et al., 2006). Furthermore, pressure solution is another possible process, being enhanced relative to calcite by aragonite's higher solubility (Morse et al., 1980). Again by comparison with friction experiments on calcite (Verberne et al., 2014a,b) and with the model for velocity-weakening behaviour of NaCl aggregates put forward by Niemeijer and Spiers (2007), we speculate that both granular flow and crystal plastic deformation, or else diffusive mass transfer, are operative and compete in the temperature range investigated, producing velocity-weakening via the mechanisms described by Niemeijer and Spiers (2007) and by Verberne et al. (2014a).

In summary, our results for the fault-derived samples show that significant quantities (~40%) of aragonite precipitated within a fault can result on the one hand to fault re-strengthening or healing due to cementation, increasing cohesion and hence frictional strength relative to sandstone-derived gouge. At the same time, aragonite precipitation can result in velocity-weakening behaviour under in-situ reservoir conditions (100 °C) leading the potential for unstable, seismogenic slip. Of course, the occurrence of velocity-weakening behaviour might be linked to a minimum quantity of aragonite versus quartz, sufficient to form a load-bearing framework that dominates the frictional behaviour (Handy, 1990). Here, we can only infer that this threshold for velocity-weakening lies at aragonite contents below 40%.

5.4. Cross-fault permeability of quartz-rich and carbonate-rich faults

Cross-fault permeability measured at room temperature showed one to 1.5 orders of magnitude decrease during shearing, from ~10^{-15} m^2 to ~10^{-17} m^2, for both sandstone-derived gouges (Fig. 4). The CO_2-exposed, carbonate-rich fault gouge, on the other hand, showed a smaller reduction in permeability, i.e. by a factor of 5 (cf. Fig. 4). The sharp, initial decrease in permeability upon shearing of the sandstone-derived samples, followed by the levelling off to more or less constant permeability values, is in good agreement with the trend seen by Zhang and Tullis (1998) in their experiments on pure quartz gouges (σ_n^{eff} = 21 MPa, 10 mm displacement). This sharp decrease is inferred to be the result of shear-enhanced gouge compaction, as grain size reduction and rearrangement of grains allow for a denser grain packing (e.g. Marone and Scholz, 1989; Zhang and Tullis, 1998). The more or less constant permeability values obtained afterwards most likely reflect the transition from shear-enhanced compaction, by optimal packing of crushed grains in the body of the sample, to localisation of gouge shearing into very thin, layer-parallel shear bands (Carpenter et al., 2016; Chen et al., 2015; Verberne et al., 2014a; Zhang and Tullis, 1998). Note that shear-enhanced compaction is more effective than compressive loading (e.g. Mandl et al., 1977), explaining the slightly larger permeability reductions seen upon re-shearing than observed after periods of static holding.

From Fig. 4, it is clear that the total reduction in cross-fault permeability for the two quartz-rich reservoir gouges is larger than for the carbonate-rich fault material. This difference is presumably related to differences in grain size reduction, compaction and localisation of shear between the quartz-rich vs. carbonate-rich gouges. However, due to the limited number of experiments conducted as well as poor preservation of the samples after removal from the sample assembly, we do not have microstructural evidence to support any particular mechanism of permeability reduction.

Finally, comparing our cross-fault permeability data for the two sandstone-derived gouges, our experiments suggest that minor mineralogical differences related to sediment variability or to long-term exposure of such materials to CO_2 will not have a major influence on the transport properties of gouge-filled faults or on how the permeability evolves with shear deformation after gouge formation associated with fault slip. Cross-fault permeabilities of the order of 10^{-17}–10^{-16} m^2 can be expected in such gouges at effective normal stresses of ~50 MPa. Our results also show that reactivated aragonite-rich (cemented) fault rock can be expected to show similar permeability at comparable conditions. We also observed that cross-fault permeability decreased in all sample materials predominantly because of accumulated shear, with little effect of time during periods of hold (Section 4.2, Fig. 4). However, during long periods of static healing under geological conditions, time-dependent, thermally-activated compaction and sealing processes will likely lead to lower permeabilities developing after fault slip then seen in our gouge shearing tests at room temperature.

5.5. Implications for fault integrity in sandstone CO_2 storage systems

5.5.1. Effects of CO_2 exposure on fault strength and slip stability

Understanding the frictional behaviour and transport properties of faults, bounding or within a reservoir, plays an important role in assessing the integrity of potential CCS sites. Our results have demonstrated that faults formed in quartz-rich sandstones (58–90% quartz) and filled with gouges of sandstone composition can be expected to show stable, velocity- strengthening sliding behaviour with an apparent friction coefficient of 0.5–0.6 under in-situ conditions. Even after long-term CO_2-exposure and gouge bleaching, the frictional strength and velocity dependent behaviour of such faults is not affected significantly, as CO_2-induced mineralogical changes are minimal due to the limited reactive mineral content of quartz-rich sandstones. Indeed the effects of reaction with CO_2, and of the associated bleaching, on rock mineralogy will often be subordinate to variations in initial composition. However, if extensive calcite or aragonite precipitation has occurred, in a leaky, degassing fault for example, then potential exists for increased cohesive strength upon slip and for unstable sliding at in-situ temperatures of >80–100 °C, both dry and in the presence of fluids. Apparent friction coefficient values in such carbonate-rich fault rock lie in the range 0.6–0.7. Extensive precipitation of carbonate minerals, as observed along the SWF, is unlikely to occur by simple CO_2 leakage from a CCS site, as large volumes of Ca-rich fluids would have to pass along the fault. However, there may be implications for carbonate-rich faults that are present within the field prior to CO_2 injection. Assuming a geothermal gradient of 20–25 °C/km, carbonate-rich fault gouges can be expected to become velocity-weakening at depths >3–4 km, and in the framework of RSF modelling then have the potential to exhibit enhanced (micro)seismicity compared with purely clastically-derived gouges, when actively slipping.

5.5.2. Permeability evolution within an active fault

Although limited, our room temperature cross-fault permeability data showed a roughly two order of magnitude decrease in permeability over only a few mm of shear displacement. These findings suggest that while fault slip may lead to initial dilational cataclasis and a significant increase in permeability, as new fault gouge is produced, this will be rapidly reduce with on-going displacement. Such faults may even become more of a barrier than a conduit with increasing shear displacement. Similarly, mature faults are assumed to have a (well-developed) internal foliation, and as a result a relatively low starting permeability and more limited potential for compaction or dilation than observed in this study. Slip of such faults will likely cause little change in permeability. What is apparent from our data is that gouges derived from the

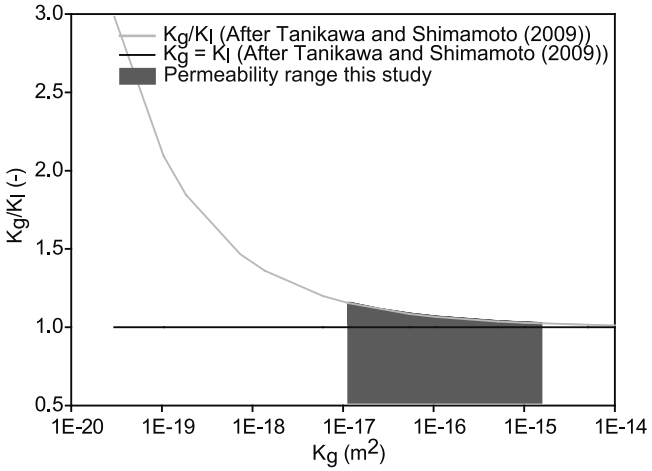

Fig. 6. Argon gas/liquid permeability ratio to liquid permeability calculated for the conditions used in our permeability tests using the relation suggested by Tanikawa and Shimamoto (2009). The κ_g/κ_l line is plotted for the mean pore pressure of 1.9 MPa used in our experiments. Based on the relation derived by Tanikawa and Shimamoto (2009), liquid permeability values for our samples are expected to be a maximum of 1.2 times lower than obtained for our argon gas permeability values. Our gas permeability values can therefore be taken as a good approximation for true permeability.

rather different simulated gouges tested show evolution to a cross-fault permeability of between 10^{-17}–10^{-16} m^2 within 2–7 mm of shearing. This suggests a likely upper bound for the transverse permeability of reactivated faults in sandstone reservoir systems.

One last point that should be noted, is that there may be a discrepancy between our argon permeability values and the cross-fault permeability to other fluids. The permeability of a porous medium represents a property that depends on material properties such as porosity, pore shape and pore size distribution. Therefore, permeability is a property of the porous medium itself, independently of fluid properties (Klinkenberg, 1941; Tanikawa and Shimamoto, 2009). However, especially at low permeability ($\kappa < 10^{-18}$ m^2), gas permeability values are generally higher than liquid permeability values (Faulkner and Rutter, 2000; Klinkenberg, 1941; Tanikawa and Shimamoto, 2009). This phenomena is known as the Klinkenberg effect and reflects the difference in interaction between gasses and liquids with the pore-walls. In the case of liquids, a thin layer of molecules adsorbs to the pore-walls, having zero velocity, whereas as in the case of gases, molecules slip along the pore-walls with a non-zero velocity, yielding higher permeability values. The relationship between the gas and liquid permeability of a medium is given by Tanikawa and Shimamoto (2009):

$$\kappa_g = \kappa_l\,[1 + \beta/P_f] = \kappa_l\,[1 + (0.15\kappa_l - 0.37/P_f)] \quad (3)$$

where κ_g is the gas permeability (m^2), κ_l is the liquid permeability (m^2), β is the Klinkenberg slip factor (Pa) and P_f is the pore pressure, defined as $\frac{1}{2}(P_{upstream} + P_{downstream})$ (Pa). Tanikawa and Shimamoto (2009) assumed that the β-factor they obtained for their experiments on sandstone samples is applicable to all rocks. Using Eq. (3) and putting $\beta = 0.15\kappa_l - 0.37$ (following Tanikawa and Shimamoto, 2009), we derived the liquid permeability expected for our samples. The results are plotted in Fig. 6 in terms of a graph of κ_g/κ_l vs. κ_g. As seen, Eq. (3) predicts that gas permeability measurements made under the conditions of our tests are expected to be a maximum factor of 1.2 higher than liquid permeability values over the range of conditions investigated. On this basis, we consider our gas permeability values for the simulated Entrada Sandstone and carbonate-rich fault gouges equally valid for CO_2-charged pore water, liquid CO_2 and supercritical CO_2, as for gaseous CO_2 or argon, assuming there are no chemical reaction effects during flow-through. It should be noted that this minor impact of the Klinkenberg effect on cross-fault permeability may be overprinted by larger-scale variations along the fault plane, which should be kept in mind when using these values for upscaling to the reservoir scale.

Finally, we note that we did not determine the along-fault permeability. While the cross-fault permeability is important for controlling lateral leakage of CO_2 from a storage reservoir, the along-fault permeability will generally control any potential leakage to overlying formations. Though the cross-fault permeability is generally one to 1.5 orders of magnitude lower than the along-fault permeability (Zhang et al., 1999), it should be kept in mind that with the current injection regulations the pressure within the reservoir will be lower than the pressure in the directly overlying formation (e.g. Marston, 2013; Verdon et al., 2013). The pressure gradient will therefore inhibit leakage up the fault, and fault leakage will rather result in fluids being transferred from the overlying rock into the reservoir.

6. Conclusions

We have performed direct shear experiments on simulated gouges derived from 1) unexposed Entrada Sandstone, 2) CO_2-exposed Entrada Sandstone and 3) carbonate-rich fault rock (40% aragonite) obtained from a CO_2-leaking/degassing fault cutting the Entrada Sandstone. The Entrada Sandstone is considered to be a good analogue for many European sandstone reservoirs considered or used for CO_2 storage. Our findings can be summarised as follows:

1) Long-term CO_2-exposure and gouge bleaching does not affect the frictional behaviour of faults significantly, as CO_2-induced mineralogical changes are minimal due to the limited reactive mineral content of quartz-rich sandstones. Simulated gouges derived from both unexposed and CO_2-exposed, Entrada Sandstone showed apparent friction coefficients typical for quartz-bearing gouges (μ = 0.50–0.7). Furthermore, the Entrada Sandstone show stable (non-seismogenic) slip behaviour prior to exposure, and remains to exhibit stable, velocity-strengthening behaviour after CO_2-exposure, under dry and wet conditions at room temperature and 100 °C. At low effective normal stresses (<25 MPa), cohesion played a significant role in controlling the shear strength of the gouge, meaning that the estimated injection pressure, and hence storage capacity, can be somewhat higher than simply expected from frictional behaviour at low effective normal stresses acting on the fault plane.
2) Simulated gouges derived from the carbonate-rich fault rock exhibited apparent friction coefficient values similar to the quartz-rich gouges (μ = 0.56–0.9). Although unlikely to occur by slow CO_2 leakage from a CCS site, if extensive calcite or aragonite precipitation would occur in a leaky, degassing fault, then the potential exists for a transition from stable sliding behaviour (room temperature, dry conditions) to velocity weakening, and hence unstable or seismogenic slip, at in-situ temperatures of >80–100 °C, both dry and in the presence of fluids. Carbonate cementation will also likely increase cohesive strength upon fault slip, especially at low σ_n^{eff} (< 25 MPa).
3) Argon gas permeability measurements on dry, unexposed and CO_2-exposed Entrada showed κ- values on the order of ~10^{-15}–10^{-16} m^2 prior to shear, decreasing to ~10^{-17} m^2 after 7 mm of displacement. The gas permeability values for the simulated Entrada Sandstone and carbonate-rich fault gouges are equally valid for CO_2-charged pore water, liquid CO_2 and supercritical CO_2, as for gaseous CO_2 or argon, assuming there are no chemical reaction effects during the flow through. However,

larger-scale variations along the fault plane, which should be kept in mind when using these values for upscaling to the reservoir scale.

Acknowledgements

This research has been carried out in the context of the CATO-2-program. CATO-2 is the Dutch national research program on CO_2 Capture and Storage technology (CCS). The program is financially supported by the Dutch government (Ministry of Economic Affairs) and the CATO-2 consortium parties. We thank Dr. Niko Kampman (Shell Global Solutions) for providing the sample material and Shell Global Solutions (Rijswijk, the Netherlands) for the allowance to publish this study. EB thanks Shell Global Solutions for providing funding for the research. ARN was funded by European Research Council starting grant SEISMIC (335915) and by the Netherlands Organisation for Scientific Research (NWO) through a VIDI grant (854.12.011).

Appendix A. Supplementary data

Supplementary data associated with this article can be found, in the online version, at http://dx.doi.org/10.1016/j.ijggc.2016.08.029.

References

Baars, D.L., Stevenson, G.M., 1981. Tectonic evolution of the Paradox Basin, Utah and Colorado, Rocky Mountains Association of Geologists Guidebook. In: Wiegand, W.L. (Ed.), Geology of the Paradox Basin. , pp. 23–31.

Bachu, S., Gunter, W.D., Perkins, E.H., 1994. Aquifer disposal of CO_2: hydrodynamic and mineral trapping. Energy Convers. Manage. 35, 269–279.

Baines, S.J., Worden, R.H., 2004. The long-term fate of CO_2 in the subsurface: natural analogues for CO_2 storage. In: Baines, S.J., Worden, R.H. (Eds.), Geological Storage of Carbon Dioxide. Geological Society of London, London, pp. 59–85.

Benson, S.M., Cook, P., Anderson, J., Bachu, S., Nimir, H.B., Basu, B., Bradshaw, J., Deguchi, G., Gale, J., von Goerne, G., Heidug, W., Holloway, S., Kamal, R., Keith, D., Lloyd, P., Rocha, P., Senior, B., Thomson, J., Torp, T., Wildenborg, T., Wilson, M., Zarlenga, F., Zhou, D., 2005. Underground Geological Storage. IPCC Special Report on Carbon Dioxide Capture and Storage, Chapter 5. Intergovernmental Panel on Climate Change. Cambridge, UK, and New York: Cambridge University Press, pp. 195–276.

Burnside, N.M., Shipton, Z.K., Dockrill, B., Ellam, R.M., 2013. Man-made versus natural CO_2 leakage: a 400 k.y history of an analogue for engineered geological storage of CO_2. Geology 41, 471–474.

Burton, E.A., Walter, L.M., 1987. Relative precipitation rates of aragonite and Mg calcite from sea water: temperature or carbonate ion control? Geology 15, 111–114.

Busch, A., Kampman, N., Hangx, S.J., Snippe, J., Bickle, M., Bertier, P., Chapman, H., Spiers, C.J., Pijnenburg, R., Samuelson, J., Evans, J.P., Maskell, A., Nicholl, J., Pipich, V., Di, Z., Rother, G., Schaller, M., 2014. The Green River natural analogue as a field laboratory to study the long-term fate of CO2 in the subsurface. Energy Procedia 63, 2821–2830.

Byerlee, J., Summers, R., 1976. A note on the effect of fault gouge thickness on fault stability. Int. J. Rock Mech. Min. Sci. Geomech. Abstr. 13, 35–36.

Carpenter, B., Collettini, C., Viti, C., Cavallo, A., 2016. The influence of normal stress and sliding velocity on the frictional behaviour of calcite at room temperature: insights from laboratory experiments and microstructural observations. Geophys. J. Int. 205, 548–561.

Chadwick, R.A., Zweigel, P., Gregersen, U., Kirby, G.A., Holloway, S., Johannessen, P.N., 2004. Geological reservoir characterization of a CO_2 storage site: the Utsira Sand, Sleipner, Northern North Sea. Energy 29, 1371–1381.

Chen, J., Verberne, B.A., Spiers, C.J., 2015. Interseismic re-strengthening and stabilization of carbonate faults by non-dieterich healing under hydrothermal conditions. Earth Planet. Sci. Lett. 423, 1–12.

Chester, F.M., 1994. Effects of temperature on friction: constitutive equations and experiments with quartz gouge. J. Geophys. Res.: Solid Earth 99, 7247–7261.

Condon, S.M., 1997. Geology of the Pennsylvanian and Permian Cutler Group and Permian Kaibab Limestone in the Paradox Basin, southeastern Utah and southwestern Colorado. In: Huffman, A.C. (Ed.), U.S. Geological Survey Bulletin; 2000 Evolution of Sedimentary Basins. Paradox Basin, Washington, DC, p. 59.

den Hartog, S.A.M., Niemeijer, A.R., Spiers, C.J., 2013. Friction on subduction megathrust faults: beyond the illite–muscovite transition. Earth Planet. Sci. Lett. 373, 8–19.

Delle Piane, C., Giwelli, A., Clennell, M.B., Esteban, L., Nogueira Kiewiet, M.C.D., Kiewiet, L., Kager, S., Raimon, J., 2016. Frictional and hydraulic behaviour of carbonate fault gouge during fault reactivation—an experimental study. Tectonophysics (in press).

Edlmann, K., Haszeldine, S., McDermott, C.I., 2013. Experimental investigation into the sealing capability of naturally fractured shale caprocks to supercritical carbon dioxide flow. Environ. Earth Sci. 70, 3393–3409.

Faulkner, D., Rutter, E., 2000. Comparisons of water and argon permeability in natural clay-bearing fault gouge under high pressure at 20 °C. J. Geophys. Res.: Solid Earth 105, 16415–16426.

Gozalpour, F., Ren, S.R., Tohidi, B., 2005. CO_2 EOR and storage in oil reservoirs. Oil Gas Sci. Technol.—Rev. IFP 60, 537–546.

Gunter, W.D., Wiwchar, B., Perkins, E.H., 1997. Aquifer disposal of CO_2-rich greenhouse gases: extension of the time scale of experiment for CO_2-sequestering reactions by geochemical modelling. Mineral. Petrol. 59, 121–140.

Haines, S.H., van der Pluijm, B.A., Ikari, M.J., Saffer, D.M., Marone, C., 2009. Clay fabric intensity in natural and artificial fault gouges: implications for brittle fault zone processes and sedimentary basin clay fabric evolution. J. Geophys. Res.: Solid Earth 114, n/a–n/a.

Handy, M.R., 1990. The solid-state flow of polymineralic rocks. J. Geophys. Res. 95, 8647–8661.

Hangx, S.J.T., Spiers, C.J., Peach, C.J., 2010a. Creep of simulated reservoir sands and coupled chemical-mechanical effects of CO_2 injection. J. Geophys. Res. 115, B09205.

Hangx, S.J.T., Spiers, C.J., Peach, C.J., 2010b. The effect of deformation on permeability development in anhydrite and implications for caprock integrity during geological storage of CO_2. Geofluids 10, 369–387.

Hangx, S., van der Linden, A., Marcelis, F., Bauer, A., 2013. The effect of CO_2 on the mechanical properties of the Captain Sandstone: geological storage of CO_2 at the Goldeneye field (UK). Int. J. Greenh. Gas Control 19, 609–619.

Hangx, S., Bakker, E., Bertier, P., Nover, G., Busch, A., 2015. Chemical–mechanical coupling observed for depleted oil reservoirs subjected to long-term CO2-exposure—a case study of the Werkendam natural CO2 analogue field. Earth Planet. Sci. Lett. 428, 230–242.

Haszeldine, R.S., Quinn, O., England, G., Wilkinson, M., Shipton, Z.K., Evans, J.B., Heath, J., Crossey, L., Ballentine, C.J., Graham, C.M., 2005. Natural geochemical analogues for carbon dioxide storage in deep geological porous reservoirs, a United Kingdom perspective. Oil Gas Sci. Technol.—Rev. IFP 60, 33–49.

Haszeldine, R.S., 2009. Carbon capture and storage: how green can black be? Science 325, 1647–1652.

Hawkes, C., McLellan, P.J., Bachu, S., 2005. Geomechanical factors affecting geological storage of CO_2 in depleted oil and gas reservoirs. J. Can. Pet. Technol. 44, 52–61.

Herzog, R.E., Shi, Q., Patil, J.N., Katz, J.L., 1989. Magnetic water treatment: the effect of iron on calcium carbonate nucleation and growth. Langmuir 5, 861–867.

Hintze, L.F., Willis, G.C., Laes, D.Y.M., Sprinkel, D.A., Brown, K.D., 2000. Digital Geologic Map of Utah: Utah Geological Survey Map 179DM, Scale 1:500,000. Utah Geological Survey.

Hirth, G., Teyssier, C., Dunlap, J.W., 2001. An evaluation of quartzite flow laws based on comparisons between experimentally and naturally deformed rocks. Int. J. Earth Sci. 90, 77–87.

Hitchon, B., 1996. Aquifer Disposal of Carbon Dioxide: Hydrodynamic and Mineral Trapping—Proof of Concept. Geoscience Publishing Ltd., Sherwood Park, Alberta, Canada.

Holloway, S., 2001. Storage of fossil fuel-derived carbon dioxide beneath the surface of the earth. Annu. Rev. Energy Environ. 26, 145–166.

Huq, F., Haderlein, S.B., Cirpka, O.A., Nowak, M., Blum, P., Grathwohl, P., 2015. Flow-through experiments on water–rock interactions in a sandstone caused by CO2 injection at pressures and temperatures mimicking reservoir conditions. Appl. Geochem. 58, 136–146.

Kampman, N., Bickle, M., Maskell, A., Chapman, H., Evans, J., Purser, G., Zhou, Z., Schaller, M., Gattacceca, J.C., Bertier, P., 2014. Drilling and sampling a natural CO_2 reservoir: implications for fluid flow and CO_2-fluid–rock reactions during CO_2 migration through the overburden. Chem. Geol. 369, 51–82.

Kampman, N., Busch, A., Bertier, P., Snippe, J., Hangx, S., Pipich, V., Di, Z., Rother, G., Harrington, J.F., Evans, J.P., Maskell, A., Chapman, H.J., Bickle, M.J., 2016. Observational evidence confirms modelling of the long-term integrity of CO_2-reservoir caprocks. Nat. Commun. 7.

Kanagawa, K., Cox, S.F., Zhang, S., 2000. Effects of dissolution-precipitation processes on the strength and mechanical behavior of quartz gouge at high-temperature hydrothermal conditions. J. Geophys. Res.: Solid Earth 105, 11115–11126.

Kearney, C., Zhao, Z., Bruet, B.J.F., Radovitzky, R., Boyce, M.C., Ortiz, C., 2006. Nanoscale anisotropic plastic deformation in single crystal aragonite. Phys. Rev. Lett. 96, 255505.

Keulen, N., Heilbronner, R., Stünitz, H., Boullier, A.-M., Ito, H., 2007. Grain size distributions of fault rocks: a comparison between experimentally and naturally deformed granitoids. J. Struct. Geol. 29, 1282–1300.

Klinkenberg, L.J., 1941. The permeability of porous media to liquids and gases. In: Drilling and Production Practice. American Petroleum Institute, New York, pp. 200–213.

Knauss, K.G., Wolery, T.J., 1989. Muscovite dissolution kinetics as a function of pH and time at 70 °C. Geochim. Cosmochim. Acta 53, 1493–1501.

Lamy-Chappuis, B., Angus, D., Fisher, Q., Grattoni, C., Yardley, B.W.D., 2014. Rapid porosity and permeability changes of calcareous sandstone due to CO_2-enriched brine injection. Geophys. Res. Lett. 41, 399–406.

Langerak, E.P.A.v., Beekmans, M.M.H., Beun, J.J., Hamelers, H.V.M., Lettinga, G., 1999. Influence of phosphate and iron on the extent of calcium carbonate precipitation during anaerobic digestion. J. Chem. Technol. Biot. 74, 1030–1036.
Le Guen, Y., Renard, F., Hellmann, R., Brosse, E., Collombet, M., Tisserand, D., Gratier, J.-P., 2007. Enhanced deformation of limestone and sandstone in the presence of high PCO_2 fluids. J. Geophys. Res. 112, B05421.
Liteanu, E., Spiers, C.J., 2009. Influence of pore fluid salt content on compaction creep of calcite aggregates in the presence of supercritical CO_2. Chem. Geol. 265, 134–147.
Liteanu, E., Spiers, C.J., de Bresser, J.H.P., 2013. The influence of water and supercritical CO_2 on the failure behavior of chalk. Tectonophysics 599, 157–169.
Luquot, L., Gouze, P., 2009. Experimental determination of porosity and permeability changes induced by injection of CO_2 into carbonate rocks. Chem. Geol. 265, 148–159.
Mair, K., Marone, C., 1999. Friction of simulated fault gouge for a wide range of velocities and normal stresses. J. Geophys. Res.: Solid Earth 104, 28899–28914.
Mair, K., Marone, C., 2001. Shear heating in granular layers. In: Mora, P., Matsu'ura, M., Madariaga, R., Minster, J.-B. (Eds.), Microscopic and Macroscopic Simulation: Towards Predictive Modelling of the Earthquake Process. Birkhäuser Basel, Basel, pp. 1847–1866.
Major, J.R., Eichhubl, P., Dewers, T.A., Urquhart, A.S., Olson, J.E., Holder, J., 2014. The Effect of CO_2-Related Diagenesis on Geomechanical Failure Parameters: Fracture Testing of CO_2-Altered Reservoir and Seal Rocks From a Natural Analog at Crystal Geyser. American Rock Mechanics Association, Utah.
Mandl, G., Jong, L.N.J., Maltha, A., 1977. Shear zones in granular material. Rock Mech. 9, 95–144.
Marone, C., Scholz, C.H., 1989. Particle-size distribution and microstructures within simulated fault gouge. J. Struct. Geol. 11, 799–814.
Marone, C., 1998. Laboratory-derived friction laws and their application to seismic faulting. Ann. Rev. Earth Planet. Sci. 26, 643–696.
Marston, P.M., 2013. Pressure profiles for CO2-EOR and CCS: implications for regulatory frameworks. Greenh. Gases Sci. Technol. 3, 165–168.
Mikhaltsevitch, V., Lebedev, M., Gurevich, B., 2014. Measurements of the elastic and anelastic properties of sandstone flooded with supercritical CO2. Geophys. Prospect. 62, 1266–1277.
Moore, D.E., Lockner, D.A., 2004. Crystallographic controls on the frictional behavior of dry and water-saturated sheet structure minerals. J. Geophys. Res. 109, B03401.
Morrow, C.A., Moore, D.E., Lockner, D.A., 2000. The effect of mineral bond strength and adsorbed water on fault gouge frictional strength. Geophys. Res. Lett. 27.
Morse, J.W., Mucci, A., Millero, F.J., 1980. The solubility of calcite and aragonite in seawater of 35% salinity at 25 °C and atmospheric pressure. Geochim. Cosmochim. Acta 44, 85–94.
Niemeijer, A.R., Spiers, C.J., 2007. A microphysical model for strong velocity weakening in phyllosilicate-bearing fault gouges. J. Geophys. Res. 112, n/a–n/a.
Niemeijer, A.R., Vissers, R.L.M., 2014. Earthquake rupture propagation inferred from the spatial distribution of fault rock frictional properties. Earth Planet. Sci. Lett. 396, 154–164.
Niemeijer, A.R., Spiers, C.J., Peach, C.J., 2008. Frictional behaviour of simulated quartz fault gouges under hydrothermal conditions: results from ultra-high strain rotary shear experiments. Tectonophysics 460, 288–303.
Nuccio, V.F., Condon, S.M., 1996. Burial and thermal history of the Paradox Basin, Utah and Colorado, and petroleum potential of the Middle Pennsylvanian Paradox Formation. In: Huffman, A.C., Lund, W.R., Godwin, L.H. (Eds.), Geology and Resources of the Paradox Basin: Utah Geological Association Guidebook. , pp. 57–76.
Ogata, K., Senger, K., Braathen, A., Tveranger, J., 2014. Fracture corridors as seal-bypass systems in siliciclastic reservoir-cap rock successions: field-based insights from the Jurassic Entrada Formation (SE Utah, USA). J. Struct. Geol. 66, 162–187.
Palandri, J.L., Kharaka, Y.K., 2005. Ferric iron-bearing sediments as a mineral trap for CO_2 sequestration: iron reduction using sulfur-bearing waste gas. Chem. Geol. 217, 351–364.
Pauwels, H., Gaus, I., Le Nindre, Y.M., Pearce, J., Czernichowski-Lauriol, I., 2007. Chemistry of fluids from a natural analogue for a geological CO_2 storage site (Montmiral, France): lessons for CO_2-water-rock interaction assessment and monitoring. Appl. Geochem. 22, 2817–2833.
Peach, C.J., 1991. Influence of Deformation on the Fluid Transport Properties of Salt Rocks, Faculty of Geosciences. Utrecht University, Utrecht, p. 238.
Pearce, J., Czernichowski-Lauriol, I., Lombardi, S., Brune, S., Nador, A., Baker, J., Pauwels, H., Hatziyannis, G., Beaubien, S., Faber, E., 2004. A review of natural CO_2 accumulations in Europe as analogues for geological sequestration. Geol. Soc. London 233, 29–41, Special Publications.
Pluymakers, A.M.H., Samuelson, J.E., Niemeijer, A.R., Spiers, C.J., 2014. Effects of temperature and CO_2 on the frictional behavior of simulated anhydrite fault rock. J. Geophys. Res.: Solid Earth 119, JB011575.
Rutter, E.H., Maddock, R.H., Hall, S.H., White, S.H., 1986. Comparative microstructures of natural and experimentally produced clay-bearing fault gouges. Pure Appl. Geophys. 124, 3–30.
Samuelson, J., Spiers, C.J., 2012. Fault friction and slip stability not affected by CO_2 storage: evidence from short-term laboratory experiments on North Sea reservoir sandstones and caprocks. Int. J. Greenh. Gas Control 11S, S78–S90.
Scholz, C.H., 1998. Earthquakes and friction laws. Nature 391, 37–41.
Scholz, C.H., 2002. The Mechanics of Earthquakes and Faulting, 2nd ed. Cambridge University Press.
Scruggs, V.J., Tullis, T.E., 1998. Correlation between velocity dependence of friction and strain localization in large displacement experiments on feldspar, muscovite and biotite gouge. Tectonophysics 295, 15–40.
Shimamoto, T., Logan, J.M., 1981. Effects of simulated clay gouges on the sliding behavior of Tennessee sandstone. Tectonophysics 75, 243–255.
Shipton, Z.K., Evans, J.P., Kirschner, D., Kolesar, P.T., Williams, A.P., Heath, J., 2004. Analysis of CO_2 leakage through 'low-permeability' faults from natural reservoirs in the Colorado Plateau, East-Central Utah. Geol. Soc. London 233, 43–58, Special Publications.
Smith, M.M., Sholokhova, Y., Hao, Y., Carroll, S.A., 2013. Evaporite caprock integrity: an experimental study of reactive mineralogy and pore-scale heterogeneity during brine-CO2 exposure. Environ. Sci. Technol. 47, 262–268.
Stumm, W., Morgan, J.J., 1981. Aquatic Chemistry. J. Wiley and Sons Inc.
Sutherland, H.J., Cave, S.P., 1980. Argon gas permeability of New Mexico rock salt under hydrostatic compression. Int. J. Rock Mech. Min. Sci. Geomech. Abstr. 17, 281–288.
Tanikawa, W., Shimamoto, T., 2009. Comparison of Klinkenberg-corrected gas permeability and water permeability in sedimentary rocks. Int. J. Rock Mech. Min. Sci. 46, 229–238.
Tembe, S., Lockner, D.A., Wong, T.-F., 2010. Effect of clay content and mineralogy on frictional sliding behavior of simulated gouges: binary and ternary mixtures of quartz, illite, and montmorillonite. J. Geophys. Res. 115, B03416.
Tenthorey, E., Cox, S.F., 2006. Cohesive strengthening of fault zones during the interseismic period: an experimental study. J. Geophys. Res.: Solid Earth 111, n/a–n/a.
Trippetta, F., Collettini, C., Barchi, M.R., Lupattelli, A., Mirabella, F., 2013. A multidisciplinary study of a natural example of a CO_2 geological reservoir in central Italy. Int. J. Greenh. Gas Control 12, 72–83.
Van der Meer, L.G.H., Kreft, E., Geel, C.R., D'Hoore, D., Hartman, J., 2006. CO_2 storage and testing enhanced gas recovery in the K12-B reservoir. In: 23rd World Gas Conference, Amsterdam, The Netherlands, p. 11.
Verberne, B.A., Plümper, O., Matthijs de Winter, D.A., Spiers, C.J., 2014a. Superplastic nanofibrous slip zones control seismogenic fault friction. Science 346, 1342–1344.
Verberne, B.A., Spiers, C.J., Niemeijer, A.R., De Bresser, J.H.P., De Winter, D.A.M., Plümper, O., 2014b. Frictional properties and microstructure of calcite-rich fault gouges sheared at sub-seismic sliding velocities. Pure Appl. Geophys. 171, 2617–2640.
Verdon, J.P., Kendall, J.-M., Stork, A.L., Chadwick, R.A., White, D.J., Bissell, R.C., 2013. Comparison of geomechanical deformation induced by megatonne-scale CO2 storage at Sleipner, Weyburn, and In Salah. Proc. Natl. Acad. Sci. 110, E2762–E2771.
Vialle, S., Vanorio, T., 2011. Laboratory measurements of elastic properties of carbonate rocks during injection of reactive CO_2-saturated water. Geophys. Res. Lett. 38, L01302.
Vialle, S., Contraires, S., Zinzsner, B., Clavaud, J.-B., Mahiouz, K., Zuddas, P., Zamora, M., 2014. Percolation of CO_2-rich fluids in a limestone sample: evolution of hydraulic, electrical, chemical, and structural properties. J. Geophys. Res.: Solid Earth 119, 2828–2847.
Wang, H.F., 2000. Theory of Linear Poroelasticity with Applications to Geomechanics and Hydrogeology. Princeton University Press.
Watson, M.N., Zwingmann, N., Lemon, N.M., Tingate, P.R., 2003. Onshore Otway Basin carbon dioxide accumulations: CO_2-induced diagenesis in natural analogues for underground storage of greenhouse gas. APPEA J. 2003, 637–653.
White, J.A., Foxall, W., 2016. Assessing induced seismicity risk at CO_2 storage projects: recent progress and remaining challenges. Int. J. Greenh. Gas Control 49, 413–424.
Wigley, M., Kampman, N., Dubacq, B., Bickle, M., 2012. Fluid-mineral reactions and trace metal mobilization in an exhumed natural CO_2 reservoir Green River, Utah. Geology 40, 555–558.
Wigley, M., Dubacq, B., Kampman, N., Bickle, M., 2013. Controls of sluggish, CO_2-promoted, hematite and K-feldspar dissolution kinetics in sandstones. Earth Planet. Sci. Lett. 362, 76–87.
Wilkinson, M., Gilfillan, S.M.V., Haszeldine, R.S., Ballentine, C.J., 2008. Plumbing the depths-testing natural tracers of subsurface CO2 origin and migration, Utah, USA. In: Grobe, M., Pashin, J.C., Dodge, R.L. (Eds.), Carbon Dioxide Sequestration in Geological Media—State of the Science. , pp. 1–16.
Zhang, S., Tullis, T.E., 1998. The effect of fault slip on permeability and permeability anisotropy in quartz gouge. Tectonophysics 295, 41–52.
Zhang, S., Tullis, T.E., Scruggs, V.J., 1999. Permeability anisotropy and pressure dependency of permeability in experimentally sheared gouge materials. J. Struct. Geol. 21, 795–806.
Zoback, M.D., Gorelick, S.M., 2012. Earthquake triggering and large-scale geologic storage of carbon dioxide. Proc. Natl. Acad. Sci. 109, 10164–10168.